Available online at www.sciencedirect.com
SCIENCE DIRECT®
Journal of Computational Physics 199 (2004) 291–316
JOURNAL OF COMPUTATIONAL PHYSICS
www.elsevier.com/locate/jcp

r-Adaptive mesh generation for shell finite element analysis

Maenghyo Cho *, Seongki Jun

School of Mechanical and Aerospace Engineering, Seoul National University, San 56-1, Shinlim-Dong, Kwanak-Ku, Seoul 151-744, Republic of Korea

Received 28 April 2003; received in revised form 21 January 2004; accepted 12 February 2004
Available online 19 March 2004

Abstract

An *r*-adaptive method or moving grid technique relocates a grid so that it becomes concentrated in the desired region. This concentration improves the accuracy and efficiency of finite element solutions. We apply the *r*-adaptive method to computational mesh of shell surfaces, which is initially regular and uniform. The *r*-adaptive method, given by Liao and Anderson [Appl. Anal. 44 (1992) 285], aggregate the grid in the region with a relatively high weight function without any grid-tangling. The stress error estimator is calculated in the initial uniform mesh for a weight function. However, since the *r*-adaptive method is a method that moves the grid, shell surface geometry error such as curvature error and mesh distortion error will increase. Therefore, to represent the exact geometry of a shell surface and to prevent surface geometric errors, we use the Naghdi's shell theory and express the shell surface by a B-spline patch. In addition, using a nine-node element, which is relatively less sensitive to mesh distortion, we try to diminish mesh distortion error in the application of an *r*-adaptive method. In the numerical examples, it is shown that the values of the error estimator for a cylinder, hemisphere, and torus in the overall domain can be reduced effectively by using the mesh generated by the *r*-adaptive method. Also, the reductions of the estimated relative errors are demonstrated in the numerical examples. In particular, a new functional is proposed to construct an adjusted mesh configuration by considering a mesh distortion measure as well as the stress error function. The proposed weight function provides a reliable mesh adaptation method after a parameter value in the weight function is properly chosen.

Keywords: *r*-Adaptivity; Shell finite element analysis; Naghdi's shell; B-spline surface

1. Introduction

Three sources generate computational errors in a finite element solution and these sources are discretization, quadrature, and discrete-solution errors. The discretization error arises because the solution is approximated by piecewise polynomials; the quadrature error because the integrals arising in the Galerkin formulation are evaluated by numerical quadrature; and discrete-solution error because the resulting discrete systems are solved only approximately. It is natural to try to diminish the total computation error

* Corresponding author. Tel.: +82-2-880-1693; fax: +82-2-886-1693.
E-mail address: mhcho@snu.ac.kr (M. Cho).

0021-9991/$ - see front matter © 2004 Elsevier Inc. All rights reserved.
doi:10.1016/j.jcp.2004.02.007

from the above-mentioned three sources. The key factors of any computational method are reliability and efficiency. Reliability indicates that the computational error should be controlled on a given tolerance level. Efficiency requires that the computational work to compute a solution within the given tolerance is essentially as small as possible. But efficiency and reliability are contrary to each other.

Mesh-adaptive methods are used to decrease the error of finite element analyses. In engineering practice, it is impossible to assess the quality of the finite element solution without applying the mesh-adaptive method. Also, mesh-adaptive methods are useful for reducing the computational cost of large-scaled structures. In general, we can classify a mesh-adaptive method into *h*-, *p*-, and *r*-adaptive method. Methods to improve the quality of the discretization such as *h*-adaptivity or the local solution using *p*-adaptivity increase the cost of the solution. While these methods may be acceptable in final engineering analysis and model verification, it is undesirable when calculating the engineering response of prototypes in the design space. The *r*-adaptive method technique does not increase the computational cost of obtaining a solution since it introduces no new additional nodes and does not increase the degree of the element basis functions. This characteristic of the *r*-adaptive method makes it ideal for performing analyses on model prototypes that require a coarse mesh to improve performance and require a sufficiently accurate analysis to make valid design decision.

There are several works on mesh generation [1–4] and its application to finite element method [5–11]. For instance, Riccius et al. [9] proposed the adaptive mesh refinement procedure for shell problems with intersections. They reduced error by combining mesh refinement and smoothing. Also, Araújo et al. [10] introduced the *h*-adaptive strategy for elastic–plastic two-dimensional finite element analysis. They generated a mesh by using the spatial decomposition technique and used an effective stress and a ratio of plastic work as a posteriori error estimation. Askes and Rodrígues-Ferran [11] splitted the domain under consideration into two subdomains to which the *r*-adaptive and *h*-adaptive strategies were applied, respectively. Recently, Huang and co-workers [12] developed an *r*-adaptive finite element method based on moving mesh PDEs and defined the error indicator using a local spatial approximation error. Also, Huang proposed several criteria for mesh adaptation based on an error function [13,14].

In the present work, the moving grid technique through cell volume deformation proposed by Liao and co-workers [15,16] is implemented for shell finite element problems. If a conventional degenerated solid shell element is used, geometrical error is generated by curvature and mesh distortion errors. The effect of mesh distortion and surface curvature errors is mixed in this case. The surface geometric error in the coarse mesh will be magnified if isoparametric interpolation is used for the surface representation. Both mesh distortion and curvature errors need to be controlled in the *r*-adaptivity strategy. Thus, *r*-adaptivity cannot be applied efficiently to shell analysis in relatively coarse mesh configurations with degenerated shell elements. On the other hand, if we can employ a high performance shell element that is relatively insensitive to mesh distortion and has geometrically exact nature, the *r*-adaptivity can be effectively applied. Thus, in the present study, we employ a high performance nine-noded Naghdi shell element, which was developed by Cho and Roh [17] and to accurately compute the surface geometry, B-spline surface tensor patch was used. *r*-Adaptivity is performed to normalize the value of the stress error estimation of elements.

The *r*-adaptivity scheme starts from the initial uniform grid. The adjusted mesh depends upon the weighting of the estimated stress error of elements in the initial mesh configuration. Elements will shrink if their stress error is relatively large compared to those of other elements and they will be expanded if the stress error is relatively small.

The rest of the paper is organized as follows. In Section 2, the cell volume deformation mapping proposed by Liao and Anderson is presented and a simple example is used to illustrate the simplicity of the present *r*-method. In Section 3, Naghdi's shell theory is presented briefly, and an assumed partial mixed strain-based variational functional is provided for nine-noded finite element shell formulations. In Section 4, a B-spline surface is introduced to approximate the geometrically exact shell surface. Several numerical examples are followed in Section 5. In particular, the weight function (considering both stress error and mesh distortion) is modified to apply cell volume deformation mapping to shell finite element analysis of a general shell surface. Finally, conclusions are given in Section 6.

2. Deformation cell mapping

In this section, we outline the cell volume deformation mapping of Liao and Anderson. This scheme was first introduced by Moser [18] in 1965 and Liao [15,16] applied this to grid-generation problems in 1991. Mesh generation has the problem of grid tangling, which occurs when the grid-generation transformation is not one-to-one. Cell volume deformation addresses problems of grid tangling by imposing certain restrictions in the formulation of a grid-generation transform to ensure that the transform is one-to-one. The grid-generation transform scheme is given as follows.

Let $\Omega \subset \mathbb{R}^2$ be a bounded region with smooth boundary $\partial\Omega$ and $f(\vec{x})$ be a smooth weight function in Ω such that $f(\vec{x}) > 0 : \Omega \to \mathbb{R}$ satisfies

$$\int_\Omega \left(\frac{1}{f} - 1\right) \mathrm{d}\Omega = 0, \tag{1}$$

where $\mathrm{d}\Omega$ is the area element. Find a one-to-one and onto transformation $\vec{\phi} : \Omega \to \Omega$ which satisfies

$$\begin{aligned} &\det \nabla \vec{\phi}(\vec{x}) = f(\vec{\phi}(\vec{x})), \quad \vec{x} \in \Omega, \\ &\vec{\phi}(\vec{x}) = \vec{x}, \quad \vec{x} \in \partial\Omega. \end{aligned} \tag{2}$$

In the above transformation, $\vec{x}$ are the coordinates of an initial grid and $\vec{\phi}$ are the coordinates of the new adapted grid. The function $f(\vec{\phi}(\vec{x}))$ is the transformation Jacobian, or in other words, the cell size of the new grid. Hence, the solution of the problem specifies the cell size distribution according to the location $\vec{\phi}(\vec{x})$ of the new grid cells. That is, if Ω is computational mesh domain, the transformation $\vec{\phi}$ contracts elements where f is small, and expands elements where f is large.

Liao and Anderson [15] give the following method to construct $\vec{\phi}$ which satisfies (2).

Step 1. Construct a vector field $\vec{v} : \Omega \to \mathbb{R}^2$ where the velocity $\vec{v}(\vec{x})$, $\vec{x} \in \Omega$ is applied to each node. $\vec{v}(\vec{x})$ must satisfy the linearized equation

$$\operatorname{div} \vec{v}(\vec{x}) = \frac{1}{f(\vec{x})} - 1, \quad \vec{x} \in \Omega, \tag{3}$$

with Neumann boundary conditions

$$\vec{n} \cdot \vec{v}(\vec{x}) = 0, \quad \vec{x} \in \partial\Omega, \tag{4}$$

$\vec{n}$ is the outward normal on the boundary $\partial\Omega$.

Step 2. The construction of a solution $\vec{v}$ of Eq. (3) is followed. Let $g = (1/f) - 1$. For a two-dimensional shell surface $(= (0,1) \times (0,1))$, let

$$G(\vec{x}) = G(x_1, x_2) = \int_0^{x_1} g(t, x_2)\, \mathrm{d}t \tag{5}$$

for $x_1, x_2 \in [0,1]$. Note that

$$G(0, x_2) = G(x_1, 0) = G(x_1, 1) = 0 \tag{6}$$

since

$$g = 0 \quad \text{on } \partial\Omega. \tag{7}$$

Also, note that

$$\int_0^1 G(1, x_2)\, \mathrm{d}x_2 = \int_0^1 \int_0^1 g(x_1, x_2)\, \mathrm{d}x_1\, \mathrm{d}x_2 = 0 \tag{8}$$

since

$$\int_{\Omega} f(\vec{x})\,\mathrm{d}x_1\,\mathrm{d}x_2 = 1. \tag{9}$$

Next, we construct a C^1 function h on $[0,1]$ such that

$$h(0) = h'(0) = h'(1) = 0, \quad h(1) = 1. \tag{10}$$

Now, we set

$$\begin{aligned} v_1(x_1,x_2) &= \int_0^{x_1} g(t,x_2)\,\mathrm{d}t - h(x_1)\int_0^1 g(t,x_2)\,\mathrm{d}t, \\ v_2(x_1,x_2) &= h'(x_1)\int_0^{x_2}\int_0^1 g(t,s)\,\mathrm{d}t\,\mathrm{d}s. \end{aligned} \tag{11}$$

Then, letting $\vec{v} = (v_1, v_2)$, we have

$$\operatorname{div}\vec{v} = g = \frac{1}{f} - 1. \tag{12}$$

To make $\vec{v}$ formally symmetric, we first interchange x_1 and x_2 in (11), then we take the average. Thus, the perturbation vector of the symmetric problem is given as,

$$\begin{aligned} v_1(x_1,x_2) &= \frac{1}{2}\left[\int_0^{x_1} g(t,x_2)\,\mathrm{d}t - h(x_1)\int_0^1 g(t,x_2)\,\mathrm{d}t + h'(x_2)\int_0^{x_1}\int_0^1 g(s,t)\,\mathrm{d}t\,\mathrm{d}s\right], \\ v_2(x_1,x_2) &= \frac{1}{2}\left[\int_0^{x_2} g(x_1,t)\,\mathrm{d}t - h(x_2)\int_0^1 g(x_1,t)\,\mathrm{d}t + h'(x_1)\int_0^{x_2}\int_0^1 g(t,s)\,\mathrm{d}t\,\mathrm{d}s\right]. \end{aligned} \tag{13}$$

Step 3. Solve, at a fixed $\vec{x} \in \Omega$, the deformation equation

$$\begin{aligned} &\frac{\mathrm{d}}{\mathrm{d}t}\vec{\varphi}(\vec{x},t) = \vec{\eta}(\vec{\varphi}(\vec{x},t),t), \quad 0 \leqslant t \leqslant 1, \\ &\vec{\varphi}(\vec{x},1) = \vec{x}, \end{aligned} \tag{14}$$

where t is an artificial time parameter and the deformation vector field $\vec{\eta}$ is defined by

$$\vec{\eta}(\vec{\varphi}(\vec{x},t),t) = \frac{\vec{v}(\vec{\varphi}(\vec{x},t))}{\{t + (1-t)g(\vec{\varphi}(\vec{x},t))\}}. \tag{15}$$

The deformation moves the grid on Ω using velocity $\vec{v}(\vec{x})$. We choose an explicit fourth-order Runge–Kutta method for a solution of the system equation (14) and (15).

Step 4. Set

$$\vec{\phi}(\vec{x}) = \vec{\varphi}(\vec{x},0). \tag{16}$$

Then $\vec{\phi}$ satisfies Eq. (3) and gives a non-degenerative grid-generating transform. $\vec{\phi}(\vec{x})$ represents the final position obtained via the deformation of the node at point $\vec{x}$. The organization of the adaptive strategy is represented by the flow chart in Fig. 1.

We demonstrate a deformation example to show the simplicity of the above method. An initial uniform mesh has 30×30 grid points, and we want to construct a coordinate transformation $\vec{\phi} : \Omega \to \Omega$ such that the adapted grid concentrates around the points with the radii $R = \{0, 0.25, 0.5\}$. The nodes are deformed to a new grid with the following prescribed cell sizes:

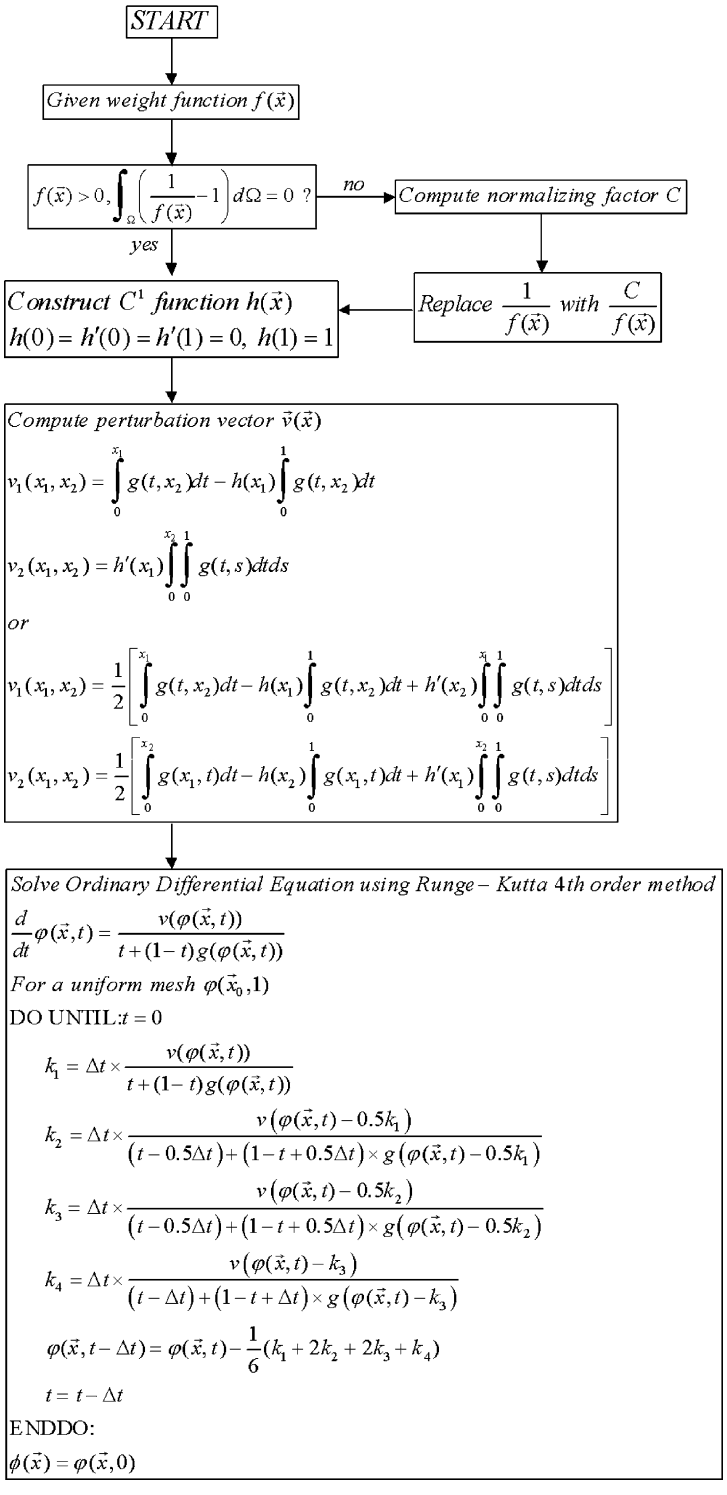

Fig. 1. Flow chart of deformation cell mapping.

$$\frac{1}{f(\vec{x})} = \{1 + \cos(8\pi \times R(\vec{x}))\},$$
$$R(x_1, x_2) = \sqrt{(x_1 - 0.5)^2 + (x_2 - 0.5)^2}. \tag{17}$$

Fig. 2 shows the magnitude of the weight function of the analytically evaluated $1/f$ in the domain $\Omega = (0,1) \times (0,1)$. Fig. 3 shows the initial uniform mesh and the final adjusted mesh after the transformation of volume deformation in the domain. It can be observed in Fig. 3 that the grid cell size is much smaller around the points $R = \{0, 0.25, 0.5\}$. Thus, the grid points aggregate in the small circle with high density.

The cell volume deformation can be applied on an L-shape domain [19,20]. Based on the weighting distribution in Fig. 2, the cell volume deformation is applied on an L-shape domain. In this case, we must modify the weight function defined from Eq. (17) because it does not satisfy Eq. (1):

$$\frac{1}{f(\vec{x})} = C \times \left\{1 + \cos(8\pi \times R(\vec{x}))\right\}, \tag{18}$$

where C is a normalizing factor for the condition of weighting function as mentioned in Eq. (1). Fig. 4 shows the initial mesh and the adjusted mesh configuration on the L-shape region. As shown in Fig. 4(b), we can obtain the adjusted mesh configuration similar to the one in Fig. 3(b).

The adjusted mesh generated by the deformation is not folded by the existence and uniqueness theorem of ordinary differential equation, which is given in Eq. (14). These examples show that the adjusted mesh yields the desired cell size characterized by the function f.

The proposed r-adaptive process needs not to be started from a uniform initial configuration. The process can be started from a distorted mesh configuration. But we does not use non-uniform mesh as the starting mesh configuration because non-uniform mesh requires extra integration effort in calculating perturbation vector given in Eq. (11) or Eq. (13) and in calculating numeric finite difference.

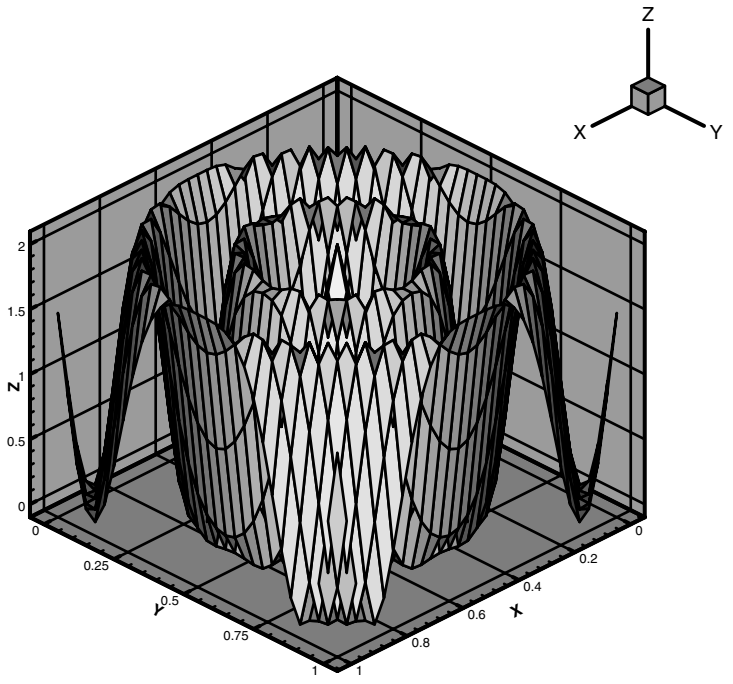

Fig. 2. Magnitude of the weight function for cell volume deformation example.

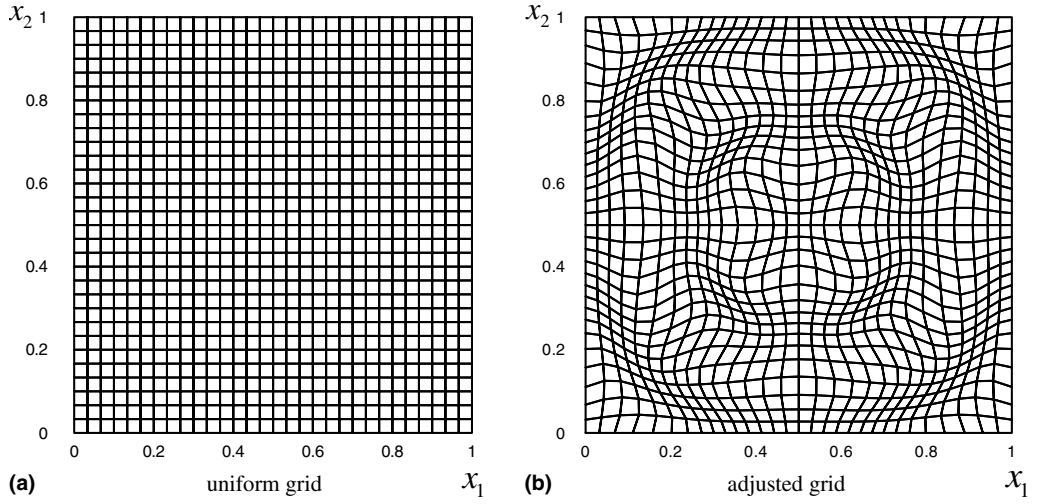

Fig. 3. (a) Initial uniform mesh and (b) adjusted mesh applied to cell volume deformation mapping on an unit square domain.

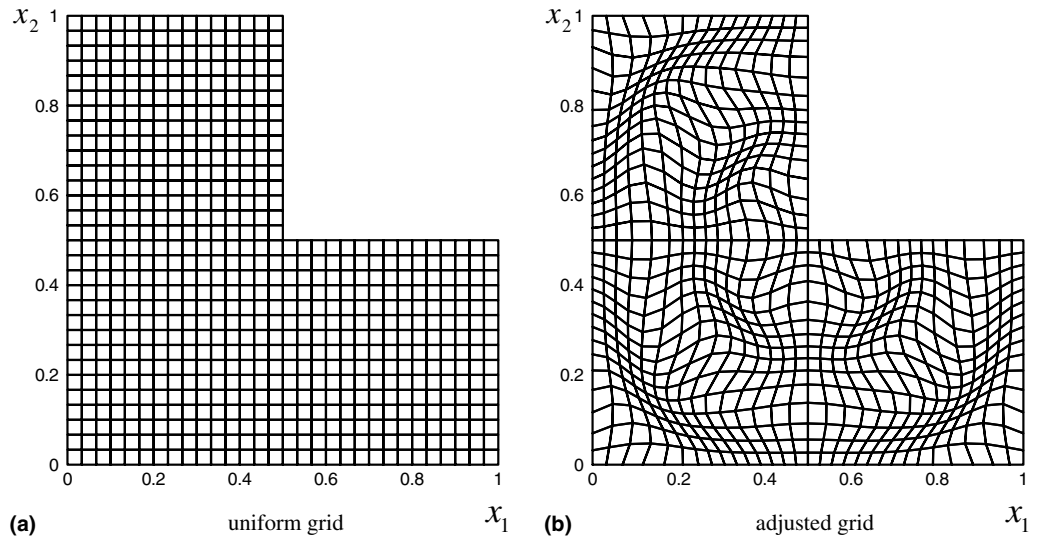

Fig. 4. (a) Initial uniform mesh and (b) adjusted mesh applied to cell volume deformation mapping on an L-shape domain.

3. Naghdis shell finite element

We employ Naghdi's shell finite element in the general curved coordinates. The element is based on the consistent first order shear deformable shell theory and the developed finite element has the geometrically exact nature. Thus, the numerical error sources are the numerical integration error and shape function approximation error. Mesh distortion effect results in quadrature errors only and does not have any influence on the pointwise curvature computations because the surface is accurately expressed by B-spline patch representation. The Naghdi's shell theory is outlined in this section and a partial mixed variational functional with independent strain measures is provided for nine-noded finite element shell formulations to reduce the locking phenomena. The detailed derivation can be founded in [17].

3.1. Kinematics of deformation and energy functional of Naghdi's shell

The kinematics of deformation of Naghdi's shell is summarized. In the convected coordinate system, the in-plane strain tensors are expressed as

$$E_{\alpha\beta} = \tfrac{1}{2}\left(g'_{\alpha\beta} - g_{\alpha\beta}\right). \tag{19}$$

To derive the strain tensors in terms of the undeformed surface tensors, deformed quantities are expressed in terms of the undeformed. The position vector $\vec{R}$ is given as

$$\vec{R} = \vec{r} + \theta^3 \vec{a}_3 \tag{20}$$

and the corresponding covariant basis vectors are

$$\vec{g}_\alpha = \frac{\partial \vec{R}}{\partial \theta^\alpha} = \frac{\partial}{\partial \theta^\alpha}(\vec{r} + \theta^3 \vec{a}_3) = \vec{a}_\alpha - b^\gamma_\alpha \vec{a}_\gamma \theta^3, \tag{21}$$

where $\vec{a}_\alpha = \vec{r}_{,\alpha}$ and b^γ_α are the tangent to the surface coordinate curve and the mixed curvature tensor components, respectively. The surface metric tensor and curvature tensor components are given as:

$$\begin{aligned} g_{\alpha\beta} &= \vec{g}_\alpha \cdot \vec{g}_\beta, \\ a_{\alpha\beta} &= \vec{a}_\alpha \cdot \vec{a}_\beta, \\ b_{\alpha\beta} &= -\vec{a}_\alpha \cdot \vec{a}_{3,\beta} = \vec{a}_3 \cdot \vec{a}_{\alpha,\beta}, \\ b^\alpha_\beta &= b_{\gamma\beta} a^{\alpha\gamma}. \end{aligned} \tag{22}$$

Thus tangent surface strain tensors are

$$E_{\alpha\beta} = \tfrac{1}{2}(g'_{\alpha\beta} - g_{\alpha\beta}) = \tfrac{1}{2}(a'_{\alpha\beta} - a_{\alpha\beta}) - (b'_{\alpha\beta} - b_{\alpha\beta})\theta^3 + \tfrac{1}{2}(b'_{\alpha\mu} b'^{\mu}_{\beta} - b_{\alpha\mu} b^{\mu}_{\beta})(\theta^3)^2. \tag{23}$$

It is assumed that $E_{\alpha\beta}$ is linear through the thickness θ^3. $E_{\alpha\beta}$ is expressed simply as follows and it can be found in [21,22]:

$$\begin{aligned} E_{\alpha\beta} &\cong \varepsilon_{\alpha\beta} + \theta^3 \omega_{\alpha\beta}, \\ \varepsilon_{\alpha\beta} &= \tfrac{1}{2}(a'_{\alpha\beta} - a_{\alpha\beta}), \\ \omega_{\alpha\beta} &= -(b'_{\alpha\beta} - b_{\alpha\beta}). \end{aligned} \tag{24}$$

Similarly, the transverse shear measure can be obtained as

$$\gamma_\alpha = 2E_{3\alpha} = (g'_{\alpha 3} - g_{\alpha 3}). \tag{25}$$

In the Naghdi's shell model, it is assumed that the transverse shear measure γ_α is constant through the thickness θ^3. Starting from Eqs. (24) and (25), we obtain the membrane, bending, and shear measures in terms of displacement, surface metric, and curvatures as follows:

$$\begin{aligned} \varepsilon_{\alpha\beta} &= \tfrac{1}{2}(u_\alpha||_\beta + u_\beta||_\alpha - 2b_{\alpha\beta} w), \\ \omega_{\alpha\beta} &= \tfrac{1}{2}\Big[\psi_\alpha||_\beta + \psi_\beta||_\alpha - b^\lambda_\alpha (u_\lambda||_\beta - b_{\lambda\beta} w) - b^\lambda_\beta (u_\lambda||_\alpha - b_{\lambda\alpha} w)\Big], \\ \gamma_\alpha &= 2E_{3\alpha} = (w_{,\alpha} + \psi_\alpha + b^\lambda_\alpha u_\lambda), \end{aligned} \tag{26}$$

where $||$ means covariant derivative in two-dimensional shell space.

From the virtual work principle of Naghdi's shell theory,

$$U = \frac{1}{2}\int_V \tau^{ij}(E_{kl})E_{ij}\,\mathrm{d}V \cong \int_\Omega \int_{-h/2}^{h/2}\left(\frac{1}{2}\tau^{\alpha\beta}E_{\alpha\beta} + \tau^{\alpha 3}E_{\alpha 3}\right)\sqrt{a}\,\mathrm{d}\theta^3\,\mathrm{d}\theta^1\,\mathrm{d}\theta^2, \tag{27}$$

where a is the determinant of the metric tensor $a_{\alpha\beta}$. τ^{ij} is the contravariant component of the stress tensor.

Using linear elastic constitutive equations:

$$\begin{aligned}\tau^{\alpha\beta} &= B^{\alpha\beta\gamma\mu}E_{\gamma\mu},\\ \tau^{\alpha 3} &= B^{\alpha 3\beta 3}E_{\beta 3}.\end{aligned} \tag{28}$$

The plane stress constitutive equations for homogeneous linear elastic isotropic materials are given in terms of the metric tensor of the shell mid surface for thin shells:

$$\begin{aligned}B^{\alpha\beta\lambda\mu} &= \frac{E}{2(1+v)}\left(a^{\alpha\lambda}a^{\beta\mu} + a^{\alpha\mu}a^{\beta\lambda} + \frac{2v}{1-v}a^{\alpha\beta}a^{\lambda\mu}\right),\\ B^{3\alpha 3\beta} &= \frac{E}{2(1+v)}a^{\alpha\beta},\end{aligned} \tag{29}$$

where E is Young's modulus and v is the Poisson's ratio.

Then, the elastic strain energy of the Naghdi's shell is given as,

$$U = \frac{1}{2}\int_\Omega \left(B^{\alpha\beta\gamma\mu}h\varepsilon_{\alpha\beta}\varepsilon_{\gamma\mu} + \frac{h^3}{12}B^{\alpha\beta\gamma\mu}\omega_{\alpha\beta}\omega_{\gamma\mu} + B^{\alpha 3\beta 3}h\gamma_\alpha\gamma_\beta\right)\sqrt{a}\,\mathrm{d}\theta^1\,\mathrm{d}\theta^2. \tag{30}$$

3.2. Hellinger–Reissner partial mixed variational formulation

In the present study, the Hellinger–Reissner partial mixed functional for the development of a shell element is employed so that the locking phenomena can be avoided. However, the Hellinger–Reissner functional for full strain and displacement fields provides a large-sized matrix inversion in each element for an assumed strain method. Cho and Roh [17] proposed the framework of partial mixed variational functional to prevent inefficient locking and constructed an independent transverse shear measure and membrane measure as variational strain parameters. The expression of the partial mixed functional is given as:

$$\begin{aligned}\Pi^P(\varepsilon_{\alpha\beta},\gamma_\alpha,u_\alpha,w,\psi_\alpha) = &\int_\Omega B^{\alpha\beta\gamma\mu}h\varepsilon_{\alpha\beta}\tfrac{1}{2}\left(u_\gamma||_\mu + u_\mu||_\gamma - 2b_{\mu\gamma}w\right)\sqrt{a}\,\mathrm{d}\theta^1\,\mathrm{d}\theta^2\\ &+\int_\Omega Gha^{\alpha\beta}\gamma_\alpha\left(w_{,\beta} + \psi_\beta + b^\lambda_\beta u_\lambda\right)\sqrt{a}\,\mathrm{d}\theta^1\,\mathrm{d}\theta^2\\ &-\frac{1}{2}\int_\Omega B^{\alpha\beta\gamma\mu}h\varepsilon_{\alpha\beta}\varepsilon_{\gamma\mu}\sqrt{a}\,\mathrm{d}\theta^1\,\mathrm{d}\theta^2 - \frac{1}{2}\int_\Omega Gha^{\alpha\beta}\gamma_\alpha\gamma_\beta\sqrt{a}\,\mathrm{d}\theta^1\,\mathrm{d}\theta^2\\ &+\frac{1}{2}\int_\Omega B^{\alpha\beta\gamma\mu}\frac{h^3}{12}\left\{\frac{1}{2}\left(\psi_\alpha||_\beta + \psi_\beta||_\alpha - b^\lambda_\beta b_{\lambda\alpha}w - b^\lambda_\alpha b_{\lambda\beta}w - b^\lambda_\alpha u_\lambda||_\beta - b^\lambda_\beta u_\lambda||_\alpha\right)\right\}\\ &\cdot\left\{\frac{1}{2}\left(\psi_\gamma||_\mu + \psi_\mu||_\gamma - b^\lambda_\gamma b_{\lambda\mu}w - b^\lambda_\mu b_{\lambda\gamma}w - b^\lambda_\gamma u_\lambda||_\mu - b^\lambda_\mu u_\lambda||_\gamma\right)\right\}\sqrt{a}\,\mathrm{d}\theta^1\,\mathrm{d}\theta^2\\ &-\int_\Omega (p^\alpha u_\alpha + pw)\sqrt{a}\,\mathrm{d}\theta^1\,\mathrm{d}\theta^2.\end{aligned} \tag{31}$$

Finite element discretizations are performed and the discretized functional is given as the following symbolic form:

$$\begin{aligned}\Pi^p\left(\vec{d},\vec{\alpha},\vec{\beta}\right) &= -\frac{1}{2}\int_\Omega \vec{\alpha}^{\mathrm{T}}\mathbf{P}_1^{\mathrm{T}}\mathbf{D}_m\mathbf{P}_1\vec{\alpha}\sqrt{a}\,\mathrm{d}\theta^1\,\mathrm{d}\theta^2 + \int_\Omega \vec{\alpha}^{\mathrm{T}}\mathbf{P}_1^{\mathrm{T}}\mathbf{D}_m\mathbf{B}_m\vec{d}\sqrt{a}\,\mathrm{d}\theta^1\,\mathrm{d}\theta^2 \\ &+\frac{1}{2}\int_\Omega \vec{d}^{\mathrm{T}}\mathbf{B}_b^{\mathrm{T}}\mathbf{D}_b\mathbf{B}_b\vec{d}\sqrt{a}\,\mathrm{d}\theta^1\,\mathrm{d}\theta^2 - \frac{1}{2}\int_\Omega \vec{\beta}^{\mathrm{T}}\mathbf{P}_2^{\mathrm{T}}\mathbf{D}_\gamma\mathbf{P}_2\vec{\beta}\sqrt{a}\,\mathrm{d}\theta^1\,\mathrm{d}\theta^2 \\ &+\int_\Omega \vec{\beta}^{\mathrm{T}}\mathbf{P}_2^{\mathrm{T}}\mathbf{D}_\gamma\mathbf{B}_\gamma\vec{d}\sqrt{a}\,\mathrm{d}\theta^1\,\mathrm{d}\theta^2 - \vec{d}^{\mathrm{T}}\cdot\vec{f} = \frac{1}{2}\vec{d}^{\mathrm{T}}\mathbf{K}_b\vec{d} - \frac{1}{2}\vec{\alpha}^{\mathrm{T}}\mathbf{H}_m\vec{\alpha} + \vec{\alpha}^{\mathrm{T}}\mathbf{G}_m\vec{d} \\ &-\frac{1}{2}\vec{\beta}^{\mathrm{T}}\mathbf{H}_\gamma\vec{\beta} + \vec{\beta}^{\mathrm{T}}\mathbf{G}_\gamma\vec{d} - \vec{d}^{\mathrm{T}}\cdot\vec{f}, \end{aligned} \tag{32}$$

where

$$\mathbf{K}_b = \int_\Omega \mathbf{B}_b^{\mathrm{T}}\mathbf{D}_b\mathbf{B}_b\sqrt{a}\,\mathrm{d}\theta^1\,\mathrm{d}\theta^2, \tag{33}$$

$$\mathbf{H}_m = \int_\Omega \mathbf{P}_1^{\mathrm{T}}\mathbf{D}_m\mathbf{P}_1\sqrt{a}\,\mathrm{d}\theta^1\,\mathrm{d}\theta^2, \tag{34}$$

$$\mathbf{G}_m = \int_\Omega \mathbf{P}_1^{\mathrm{T}}\mathbf{D}_m\mathbf{B}_m\sqrt{a}\,\mathrm{d}\theta^1\,\mathrm{d}\theta^2, \tag{35}$$

$$\mathbf{H}_\gamma = \int_\Omega \mathbf{P}_2^{\mathrm{T}}\mathbf{D}_\gamma\mathbf{P}_2\sqrt{a}\,\mathrm{d}\theta^1\,\mathrm{d}\theta^2, \tag{36}$$

$$\mathbf{G}_\gamma = \int_\Omega \mathbf{P}_2^{\mathrm{T}}\mathbf{D}_\gamma\mathbf{B}_\gamma\sqrt{a}\,\mathrm{d}\theta^1\,\mathrm{d}\theta^2, \tag{37}$$

where $\vec{f}$ is the element nodal vector and $\vec{d}$ is the nodal displacement vector. The column vectors $\vec{\alpha}$ and $\vec{\beta}$ are membrane and shear strain parameters, respectively.

4. Shell with B-spline surfaces

This section presents the definition, important properties and manipulations of B-spline surface [23,24] which are to generate general surfaces of the shells. They can provide geometrically exact and CAD-generated free-form surface representations. The free-form surfaces by B-spline are employed to model the shell surfaces geometrically in the present study.

A B-spline curve is defined by the following equation:

$$C(t) = \sum_{i=0}^{n} N_{i,p}(t)P_i, \tag{38}$$

where $N_{i,p}(t)$ are B-spline basis functions, P_i are vectors composed of x, y, z coordinates of the control points, p(degree + 1) is the order of a B-spline curve, and $[t_0, t_1, t_2, \ldots, t_{n+p}]$ is the knot vector which specifies the distribution of the parameter t along the curve. The relationship between the order of the curve p, the number of control points $n+1$, and the number of knots $m+1$ is given by

$$m = n + p. \tag{39}$$

B-spline basis functions $N_{i,p}(t)$ are also called B-spline blending functions and are defined by

$$N_{i,1}(t) = \begin{cases} 1 & \text{if } t_i \leqslant t < t_{i+1}, \\ 0 & \text{otherwise,} \end{cases} \tag{40}$$

$$N_{i,p}(t) = \frac{t - t_i}{t_{t+p+1} - t_i} N_{i,p-1}(t) + \frac{t_{i+p} - t}{t_{t+p} - t_{i+1}} N_{i+1,p-1}(t). \tag{41}$$

The interval $[t_i, t_{i+1}]$ is called the ith knot span. A knot vector is non-periodic if the first and last knots are repeated with multiplicity $p+1$, $T = \{t_0, \ldots, t_0, t_{p+1}, \ldots, t_{n-p-1}, t_n, \ldots, t_n\}$. For most practical applications, $t_0 = 0$ and $t_n = 1$. Further, a knot vector is called uniform if the knots are equally spaced. Otherwise, the knot vector is non-uniform. Non-uniform knot vectors offer greater flexibility for various design application.

B-spline curves have nice properties suitable for computer aided geometric design. These properties can be generalized as, affine invariance, convex hull, and local control properties.

As an extension of a parametric B-spline curve, a biparametric B-spline surface can be defined as the tensor product of B-spline curves. A $(p \times q)$th order B-spline surface is defined as follows:

$$S(u,v) = \sum_{i=0}^{m} \sum_{j=0}^{n} V_{i,j} M_{j,q}(v) N_{i,p}(u) \quad \left(u_{p-1} \leqslant u \leqslant u_{m+1}, v_{p-1} \leqslant v \leqslant v_{n+1}\right), \tag{42}$$

where $(m+1) \times (n+1)$ control points $V_{i,j}$ build up the control net in 3D, and $N_{i,p}(u), M_{i,q}(v)$ are the B-spline basis functions of order p and q in the u and v directions, respectively.

5. Numerical examples

In this section, we present the results of several numerical computations performed for sample problems using the method of deformation cell mapping described in Section 2. The models for the benchmark problems are cylinder, hemisphere, and torus, which are approximated by B-spline function. The weight functions of the examples are the values of pointwise stress error estimation. The stress error can be reduced by moving the nodes of the mesh. We consider the value of the stress error estimation as the weight function of the cell deformation mapping. But, in general, the weight function does not satisfy Eq. (1). Thus it is modified in the following form:

$$g(\vec{x}) = \frac{1}{f(\vec{x})} - 1 = \frac{C_s \times \Lambda_{\text{local}}}{\Lambda_{\max}}, \tag{43}$$

where Λ_{local} is the local pointwise stress error estimation value, $\Lambda_{\max}$ the maximum stress error estimation value and C_s the normalizing factor. In Eq. (43), $g(\vec{x})$ is almost equal to C_s in the region where stress error estimation value is very large. In contrast, $g(\vec{x})$ becomes nearly zero if the stress error is very small. Therefore, the grids concentrate in the area where the stress error is relatively large. The detailed expression of Λ is given at the end of this section.

This work shows linear application. It means that under the given weighting function (pointwise stress error estimation value), the deformation cell mapping determines an improved mesh configuration. The weight function should be repeatedly evaluated for the newly determined mesh configuration in order to be a nonlinear iterative process. New adjusted mesh needs to be constructed successively until the weight function becomes uniformly distributed in the domain. But this repeated process has not been done in the this study [25,26].

Also, we calculate the relative percentage error to compare the errors of the solutions evaluated in the uniform mesh and in the adjusted mesh, respectively [27]. The energy norm of the error of the finite element E_i,

$$\|\mathbf{e}\|_{E_i} = \left[\int_{E_i} (\sigma - \sigma_h)^{\mathrm{T}} \mathbf{C}^{-1} (\sigma - \sigma_h) \, \mathrm{d}\Omega \right]^{1/2} \tag{44}$$

is approximated by the value $\|\mathbf{e}\|^*_{E_i}$,

$$\|\mathbf{e}\|^*_{E_i} = \left[\int_{E_i} (\sigma^* - \sigma_h)^{\mathrm{T}} \mathbf{C}^{-1} (\sigma^* - \sigma_h) \, \mathrm{d}\Omega \right]^{1/2}, \tag{45}$$

where $\mathbf{C}$ is the material stiffness tensor, $\mathbf{e}$ the error of finite element solution, σ the exact stress tensor, σ_h the finite element stress and σ^* the improved finite element stress tensor.

If the exact stress σ are not known, the improved finite element stress tensor σ^* must replace the unknown exact stress tensor σ. For evaluating the improved finite element stresses Zienkiewicz–Zhu's least-square-fit approach [28] were used in the present study.

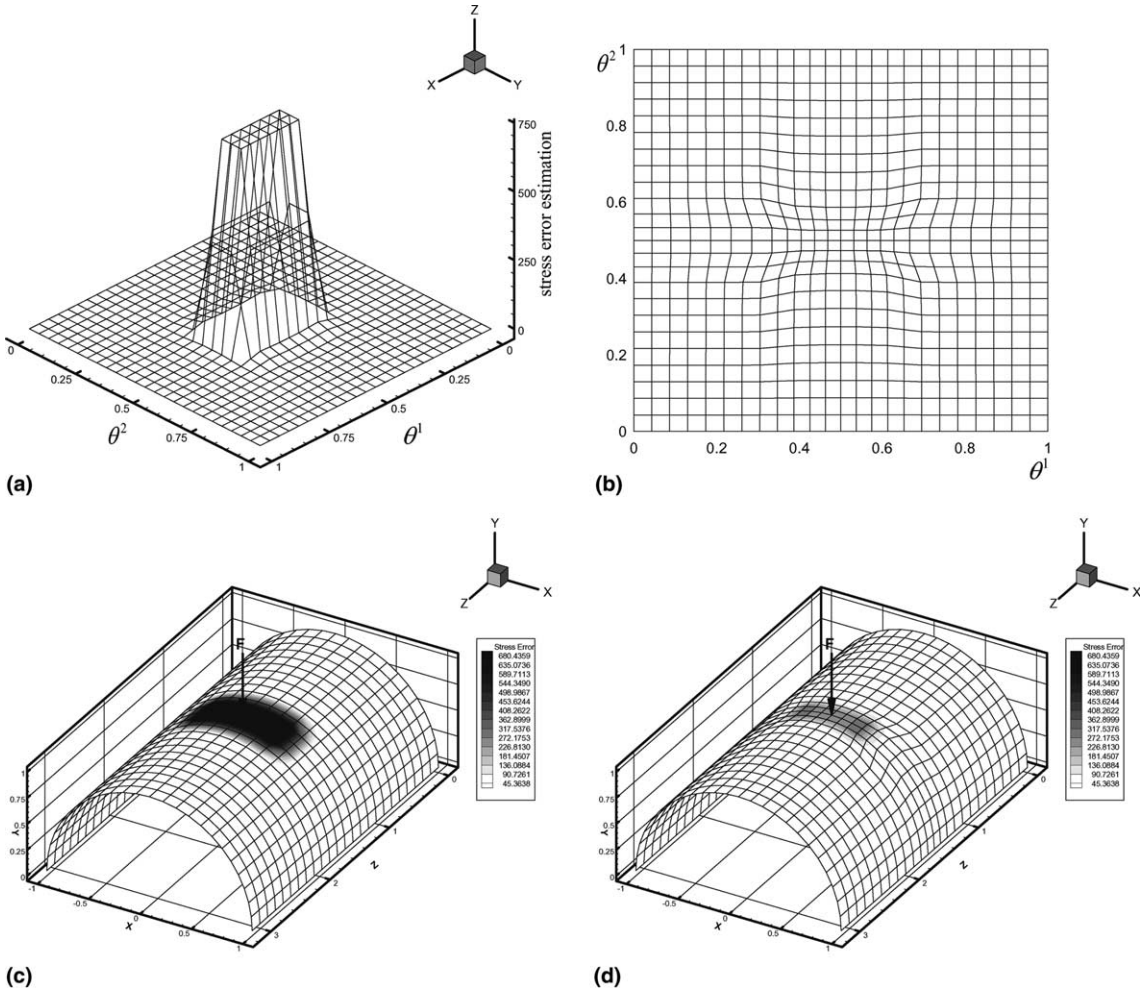

Fig. 5. Example of cylindrical shell under concentrated loads (mesh configurations and contour of stress error estimation): (a) magnitude of stress error estimation, (b) adjusted mesh in parametric domain, (c) uniform mesh on cylindrical shell and contour of stress error estimation and (d) adjusted mesh on cylindrical shell and contour of stress error estimation.

By summing up the energy contribution by each element, the energy error of the whole domain can be obtained as follows:

$$\|\mathbf{e}\|^{*2} = \sum_{i=1}^{m} \|\mathbf{e}\|_{E_i}^{*2}. \tag{46}$$

The relative percentage error is defined as follows:

$$\eta = \frac{\|\mathbf{e}\|^{*}}{\|\mathbf{u}\|} \times 100 = \frac{\left[\int_{\Omega} (\sigma^{*} - \sigma_h)^{\mathrm{T}} \mathbf{D}^{-1} (\sigma^{*} - \sigma_h)\, \mathrm{d}\Omega\right]^{1/2}}{\left[\int_{\Omega} \sigma^{*\mathrm{T}} \mathbf{D}^{-1} \sigma^{*}\, \mathrm{d}\Omega\right]^{1/2}}, \tag{47}$$

where $\mathbf{u}$ is the displacement.

The ith component of stress σ_i^p in a patch is interpolated as

$$\sigma_i^p = \mathbf{p}(x, y)\mathbf{a}_i, \quad i = 1, 2, \ldots, m, \tag{48}$$

where m is the number of stress components, $\mathbf{p}(x, y)$ is a vector of polynomials and $\mathbf{a}_i$ is the set of unknown coefficients for the ith component of stress. The coefficient $\mathbf{a}_i$ are determined by solving the following minimization problem:

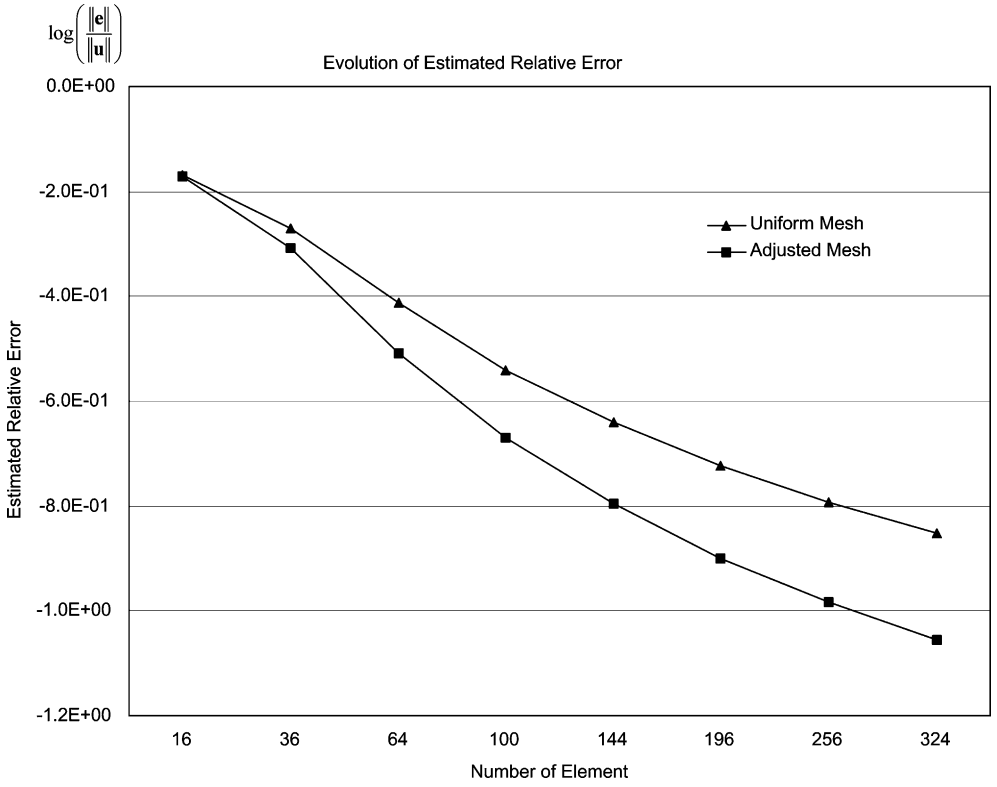

Fig. 6. Convergence of estimated relative error for cylindrical shell under concentrated loads.

$$\min\left(\sum_{k=1}^{n}\left(\sigma_i^h(x_k,y_k)-\mathbf{p}(x_k,y_k)\mathbf{a}_i\right)^2\right), \tag{49}$$

where n is the number of superconvergent stress points in the patch (SSP) and σ_i^h the ith component of stress at SSP in the FE mesh. This linear least-square problem is solved using the following Euler equations:

$$\sum_{k=1}^{n}\mathbf{p}^{\mathrm{T}}(\mathbf{x}_k)\mathbf{p}(\mathbf{x}_k)\mathbf{a}_i=\sum_{k=1}^{n}\mathbf{p}^{\mathrm{T}}(\mathbf{x}_k)\sigma_i^h(\mathbf{x}_k). \tag{50}$$

After determining the vectors $\mathbf{a}_i$ given by Eq. (50), the co-ordinates of the searched stress point are combined with Eq. (49) in order to get the improved stress value at the nodes:

$$\sigma_i^*=\mathbf{p}(x_{\mathrm{node}},y_{\mathrm{node}},z_{\mathrm{node}})\mathbf{a}_i. \tag{51}$$

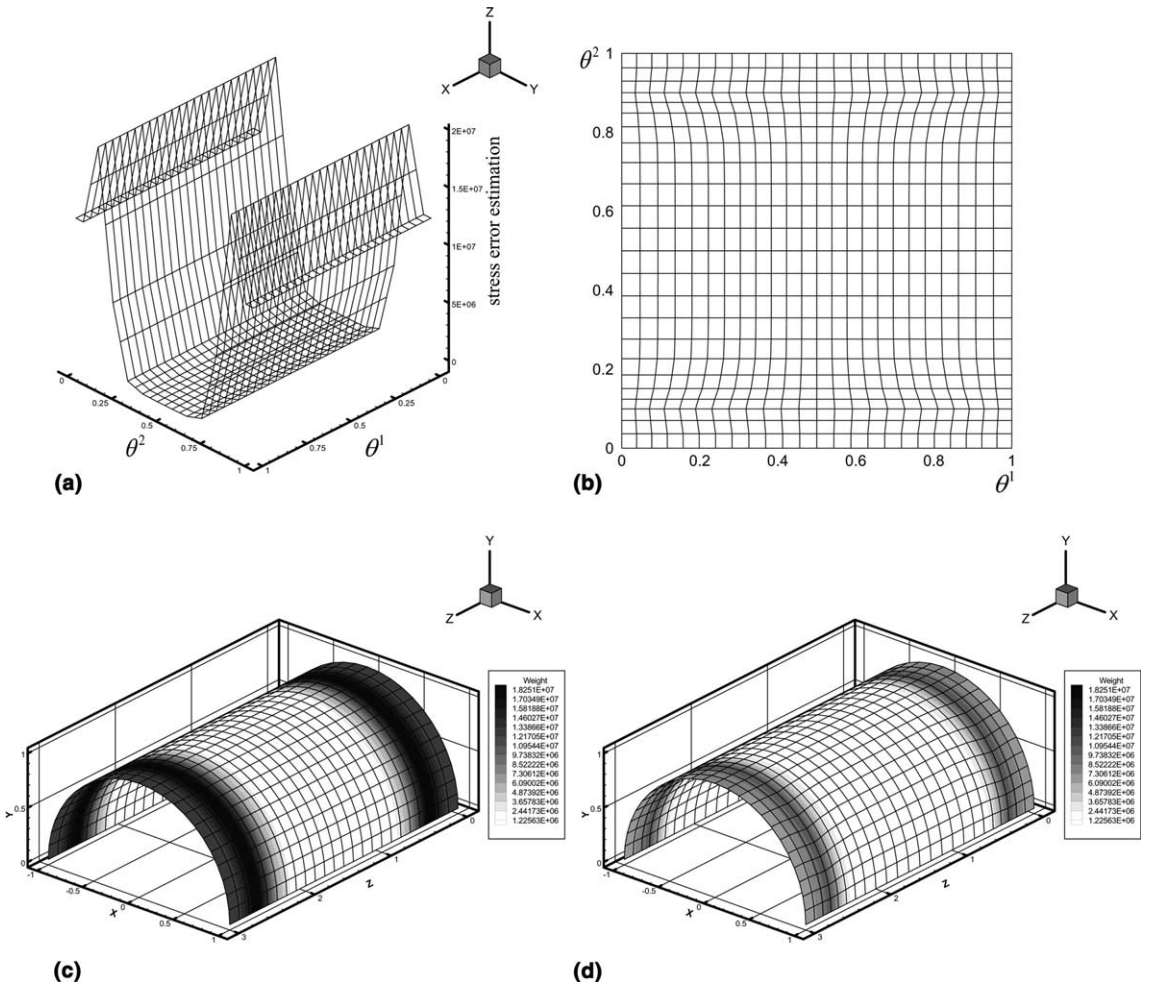

Fig. 7. Example of cylindrical shell under uniform internal pressure (mesh configurations and contour of stress error estimation): (a) magnitude of stress error estimation, (b) adjusted mesh in parametric domain, (c) uniform mesh on cylindrical shell and contour of stress error estimation and (d) adjusted mesh on cylindrical shell and contour of stress error estimation.

Then, the pointwise stress error estimation value, Λ, is calculated for the examples in the next section.

$$\Lambda = \sigma_i^* - \sigma_i^h. \tag{52}$$

5.1. Cylindrical shell

5.1.1. Cylindrical shell under concentrated loads

The first example is a pinched cylinder with rigid diaphragmed ends. Transverse loads in the radial direction are applied at the mid-section of the cylinder (see Fig. 5(c)). The magnitude of the stress error estimator evaluated in initial uniform mesh is shown in Fig. 5(a). *Adjusted mesh* in the plotting indicates the results of the proposed *r*-method. Using the stress error estimator in the uniform mesh as a weight function, the adjusted mesh can be constructed in the parametric domain (θ^1, θ^2) such that the grids are concentrated near the point in which the loads are applied without mesh tangling as shown in Fig. 5(b). Figs. 5(c) and (d) show the mesh configurations, respectively, which were mapped onto the cylindrical shell surface by the cylinder position vector. We can effectively diminish the error values where the point load is applied by using a distorted adjusted mesh given by the moving grid method as shown in Fig. 5(d).

To assess the convergence rate of the proposed *r*-adaptive method and compare it to those of the uniform refinements, the estimated relative error is calculated in each mesh configuration. Fig. 6 shows the estimated relative error of a pinched cylinder under concentrated load. The *x*-axis indicates the number of the elements for analysis and *y*-axis is the value of the estimated relative error in a logarithmic scale. As shown in Fig. 6, the *r*-method shows a much faster convergence that the uniform mesh refinement. For example, the results of the adjusted mesh with 144 elements show higher performance than the uniform mesh with 256 elements.

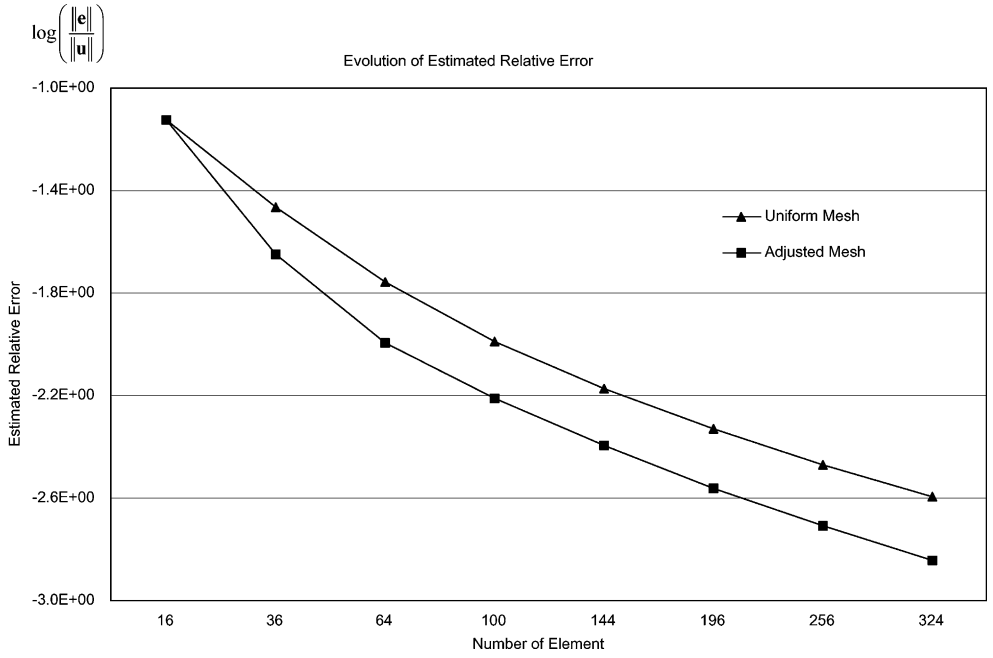

Fig. 8. Convergence of estimated relative error for cylindrical shell under uniform internal pressure.

5.1.2. Cylindrical shell under uniform internal pressure

The next example is for the cylindrical shell under uniform internal pressure. In Fig. 7(b), the refined final mesh is shown and the consistent stress error estimation is as shown in Fig. 7(a). As shown in Figs. 7(a) and (c), the value of stress error estimation is relatively large at both ends of the cylinder under uniform internal pressure. Fig. 7(d) shows that the grid shrinks at both ends having large stress error and the stress error decreases significantly after the grid shrinks.

The estimated relative error of the cylindrical shell under uniform internal pressure is depicted in Fig. 8. Similar to the case under concentrated load, Fig. 8 also shows the relative error decreases when the adjusted mesh by *r*-method is applied. Though the decreasing rate of relative error seems to be less than that of the

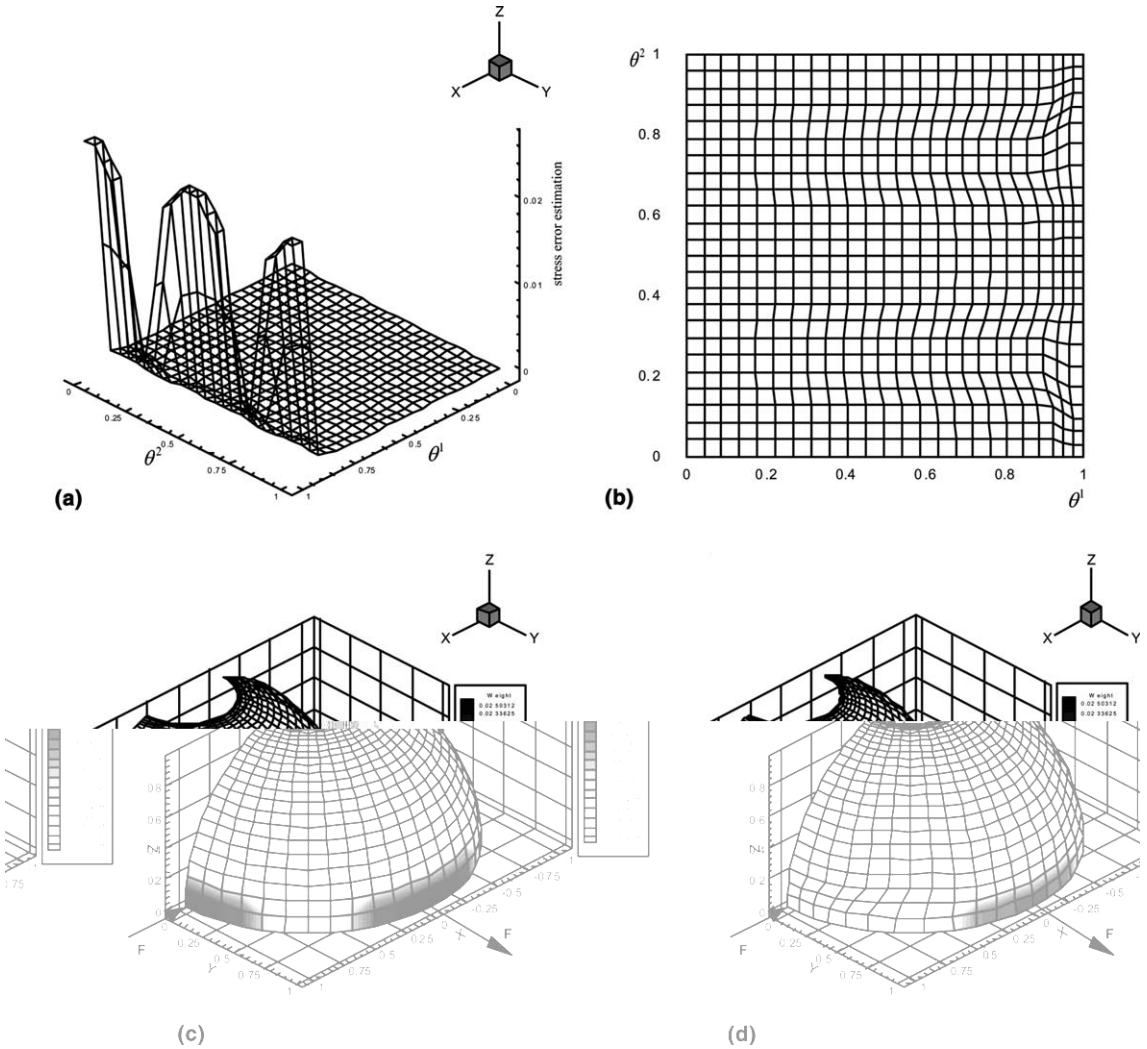

Fig. 9. Example of hemisphere under concentrated loads (mesh configurations and contour of stress error estimation): (a) magnitude of stress error estimation, (b) adjusted mesh in parametric domain, (c) uniform mesh on hemisphere and contour of stress error estimation and (d) adjusted mesh on hemisphere and contour of stress error estimation.

case under concentrated load, a considerable amount of improvement on the relative stress error with the adjusted mesh by *r*-method is shown in Fig. 8.

5.2. Spherical shell

5.2.1. Spherical shell under concentrated loads

A doubly curved spherical shell example is given in this section. The equator of the shell is chosen as a free edge. The problem reduces to a hemisphere with four point loads alternating in sign at 90° intervals along the equator as shown in Fig. 9(c). This case is similar to the pinched-cylinder because the stress error increases at the load points. The nodes are moving on the area that has a large stress error value, as shown in Fig. 9(b). Because, the finite cell size decreases at the loaded point, the stress error also decreases. Fig. 9(d) shows the improvement of the stress error estimation in the adjusted mesh configuration.

Figs. 9 and 10 show the mesh convergence for analyses in the adjusted mesh configuration. The solid line connected by the triangular marks indicates the estimation of the relative error calculated from the uniform mesh, and the solid line connected by the square marks is calculated from the adjusted mesh. The *r*-adaptive method is more useful than the uniform refined method because it significantly decreases the solution errors. From Fig. 10, it can be concluded that the *r*-adaptive method leads to higher accuracy than the uniform mesh does.

5.2.2. Hemisphere under uniform internal pressure

The hemisphere under the uniform internal pressure is considered. Fig. 11(a) shows the magnitude of the stress error estimator. The adjusted mesh in the parametric domain is shown in Fig. 11(b). The stress error estimator calculated on the uniform mesh is depicted in Figs. 11(c) and (e). It is not easy to recognize how

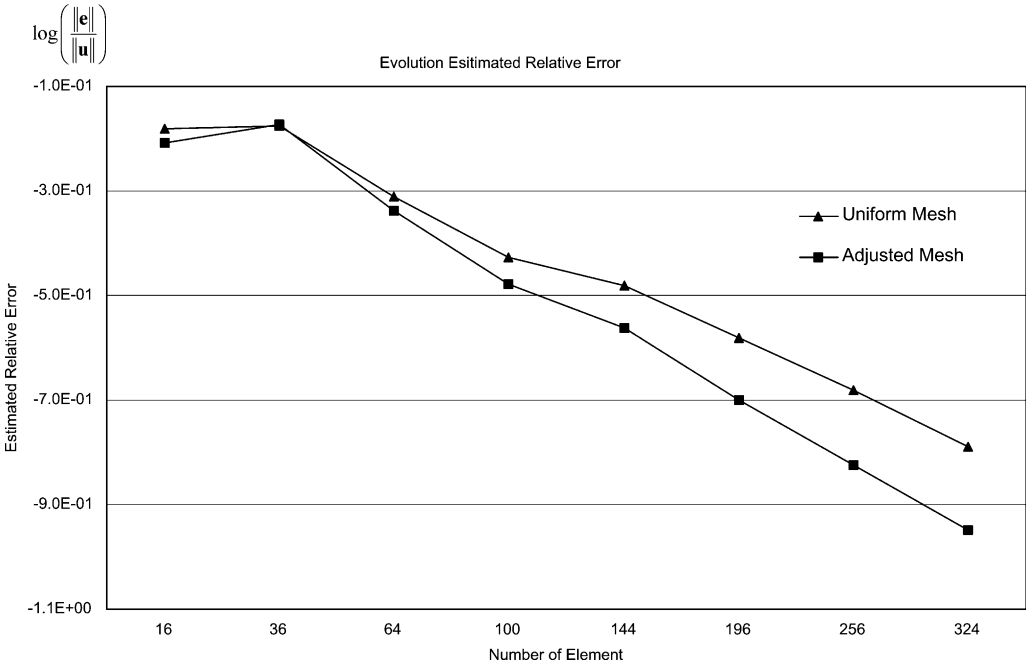

Fig. 10. Convergence of estimated relative error for hemisphere under concentrated loads.

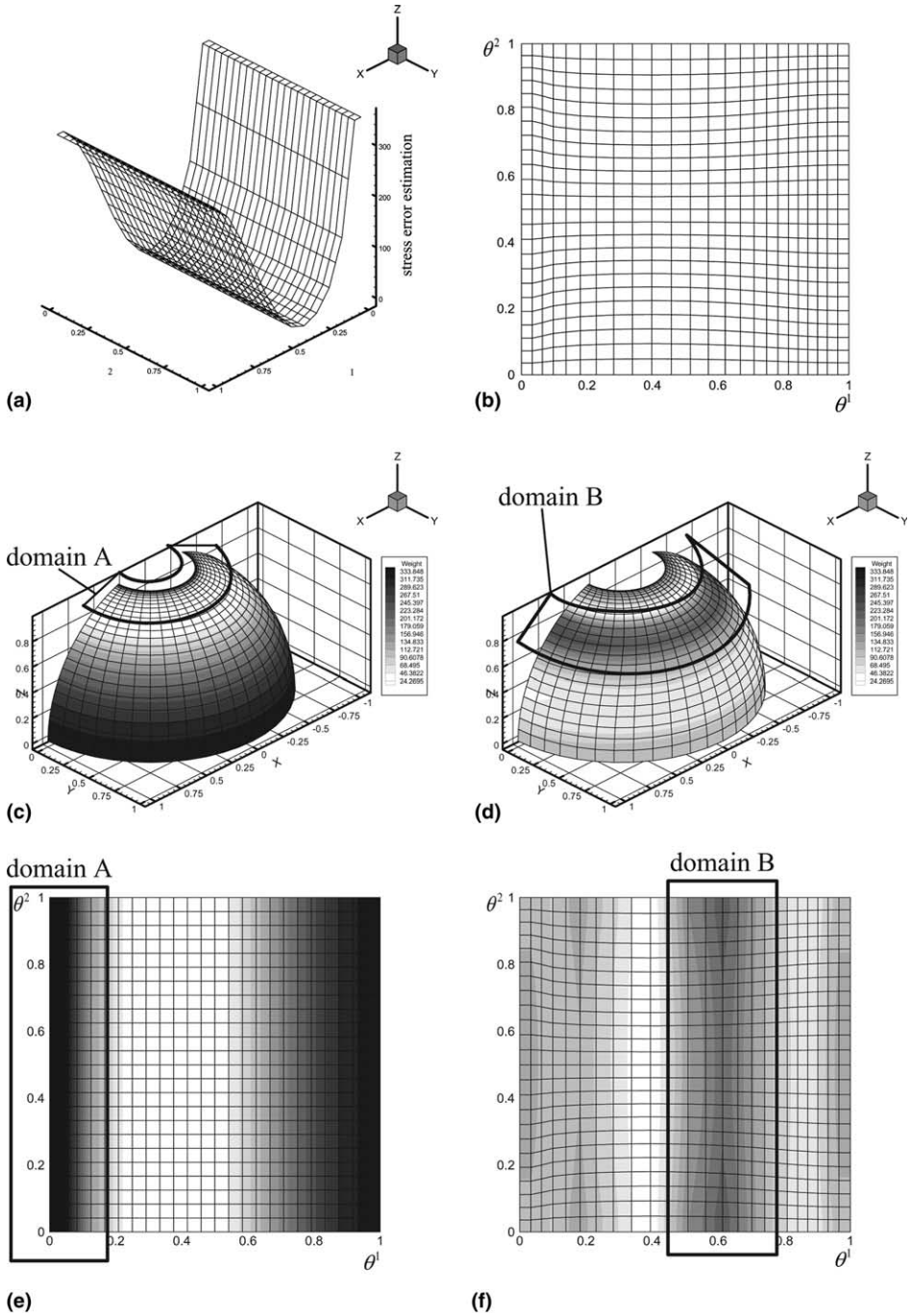

Fig. 11. Example of hemisphere under uniform internal pressure (mesh configurations and contour of stress error estimation): (a) magnitude of stress error estimation, (b) adjusted mesh in parametric domain, (c) uniform mesh on hemisphere and contour of stress error estimation, (d) adjusted mesh on hemisphere and contour of stress error estimation, (e) uniform mesh in parametric domain and contour of stress error estimation and (f) adjusted mesh in parametric domain and contour of stress error estimation.

large the stress error is because the mesh density near to the zenith (domain A) is so large. As shown in Figs. 11(c) and (e), the stress error is larger than at both upper and lower areas. Figs. 11(d) and (f) show the stress error calculated on the adjusted mesh. As in the previous examples, the grids come together at the place of high stress error value. In the adjusted mesh, the stress error value decreases. On the other hand, domain B in Figs. 11(d) and (f) has a lower stress error in the initial mesh configuration than in the adjusted mesh, but

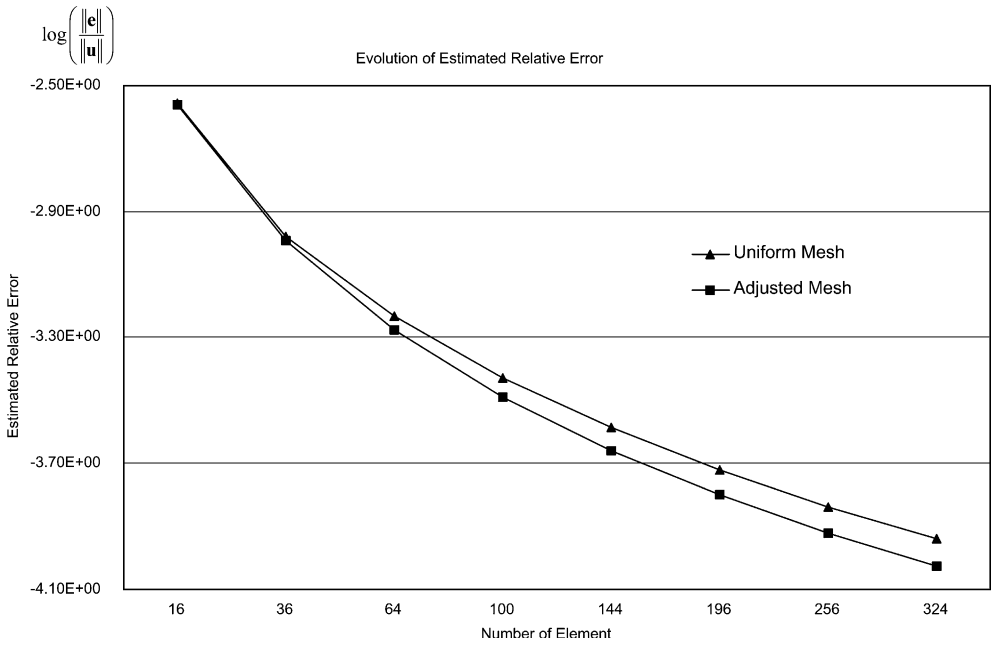

Fig. 12. Convergence of estimated relative error for hemisphere under uniform internal pressure.

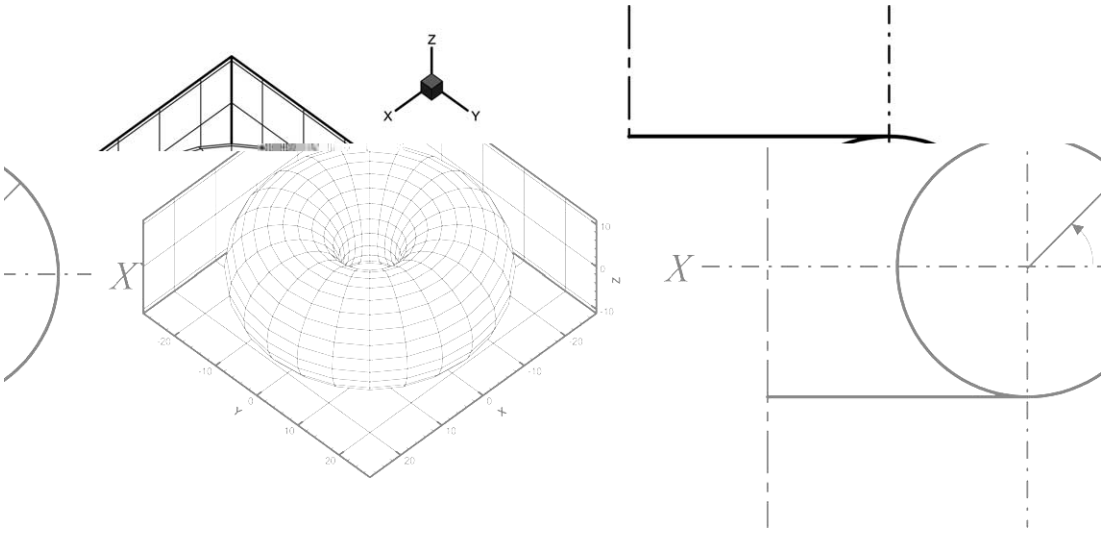

Fig. 13. The geometry of torus.

we are aware that the stress error value is raised in the adjusted mesh because of the expansion of the cell size there. However, considering all these factors, the global stress error of the overall domain becomes small.

Fig. 12 is the graph of the relative error of hemisphere under uniform internal pressure. The relative error of adjusted mesh is lower than that of uniform mesh case.

5.3. Torus under uniform internal pressure

In this problem, the *r*-adaptive method is applied to a torus subjected to a uniform internal pressure. The geometry of the torus is shown in Fig. 13. Because of the symmetry with respect to the plane *XX* in Fig. 13, the analysis is carried out from 0° to 180°. As shown in Fig. 14, the grids are concentrated on the area where

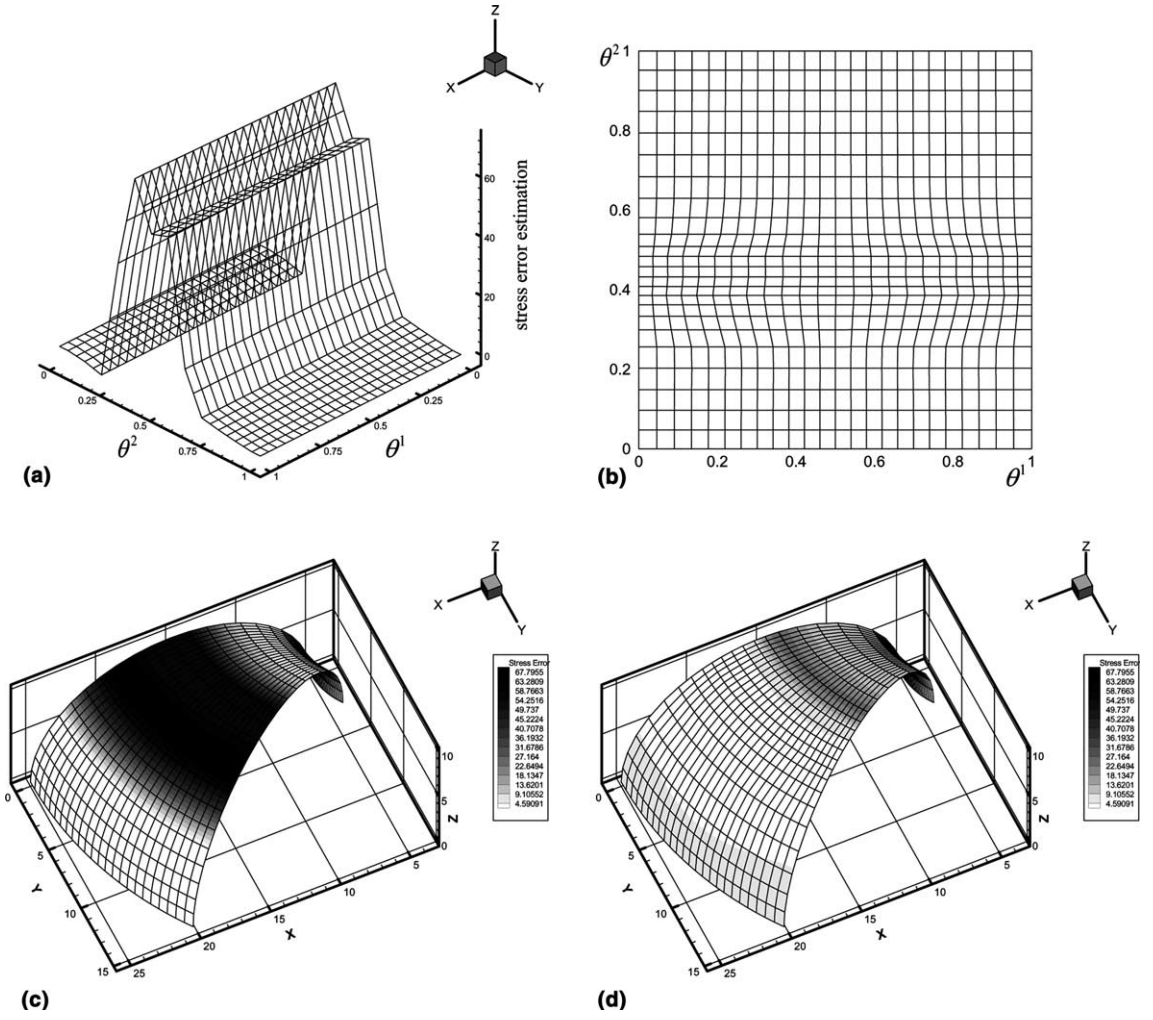

Fig. 14. Example of torus under uniform internal pressure (mesh configurations and contour of stress error estimation): (a) magnitude of stress error estimation, (b) adjusted mesh in parametric domain, (c) uniform mesh on torus and contour of stress error estimation, (d) adjusted mesh on torus and contour of stress error estimation.

there is a large stress error estimation value. Also, like previous examples, the stress error is reduced in the adjusted mesh configuration. The result of relative error of torus is plotted in Fig. 15. But special attention should be given so that the estimated relative errors calculated from the adjusted mesh with 64 elements and 100 elements are higher than those from the uniform mesh. The torus has saddle points, where the sign of the Gaussian curvature suddenly changes. That is, the torus is sensitive to the mesh distortion near the apex line where the sign of the Gaussian curvature changes.

Thus the measure of mesh distortion and the weight function of cell deformation mapping is modified to consider both effects from the stress error and from the mesh distortion. In the subsequent section, the error measure of the mesh distortion is discussed and the weight function for error estimation is modified.

5.3.1. Distortion measure

Let $l : M \to N$ be a mapping from surface M to surface N. X and x denote the local coordinates on M and N, respectively. To find the distortion measure, we consider a symmetric positive semi-definite quadratic form

$$\mathbf{Q} = \mathbf{F}^{\mathrm{T}}\mathbf{H}\mathbf{F}\mathbf{G}^{-1}, \tag{53}$$

where $\mathbf{H}$ and $\mathbf{G}$ are a first fundamental form on M and N, respectively, and $\mathbf{F}(=\frac{\partial x}{\partial X})$ is a deformation gradient matrix. Its eigenvlaues and eigenvectors define an ellipsoid. The distortion measure can be obtained by using the ratio of the maximum to minimum eigenvalue of $\mathbf{Q}$ such as

$$\Delta = \frac{\lambda_{\max}}{\lambda_{\min}}, \tag{54}$$

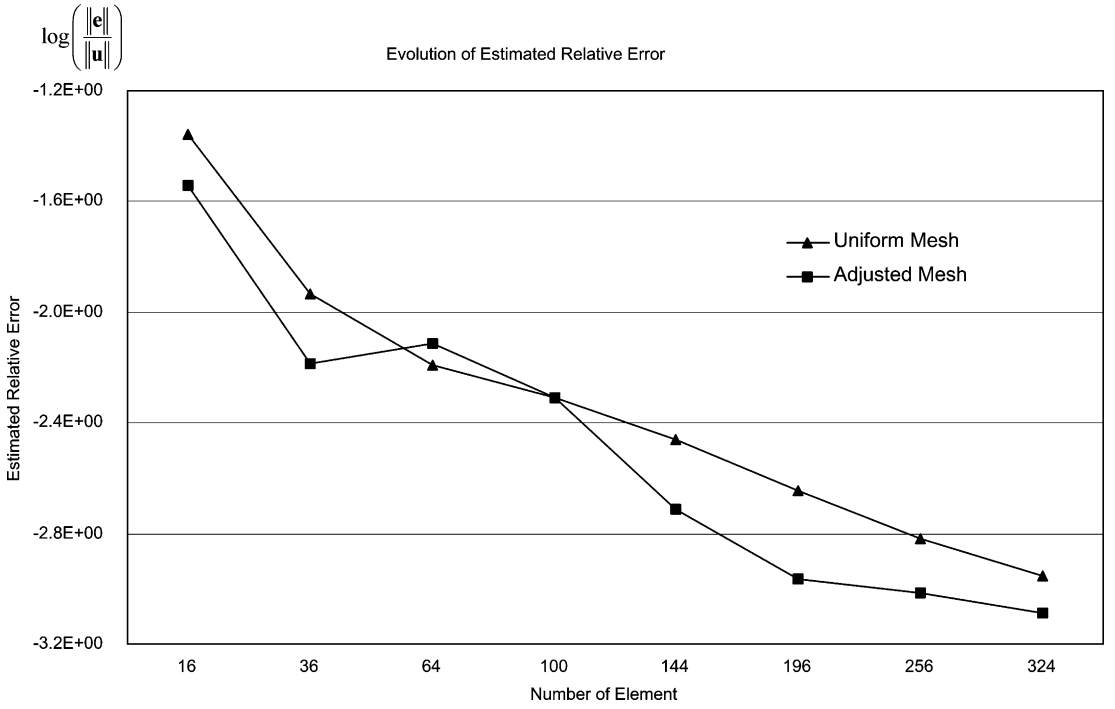

Fig. 15. Convergence of estimated relative error for torus under uniform internal pressure.

where $\lambda_{\max}$ and $\lambda_{\min}$ are the maximum and minimum of eigenvalues of $\mathbf{Q}$. If $\lambda_{\max} = \lambda_{\min}$ then ellipsoid is a perfect circle, which implies no distortion.

Reflecting the mesh distortion effect, the weight function can be written as similar to Eq. (43):

$$\left(\frac{1}{f(\vec{x})} - 1\right)_{\text{distortion}} = \frac{C_d \times \Delta_{\max}}{\Delta_{\text{local}}}, \tag{55}$$

where C_d is a normalizing factor.

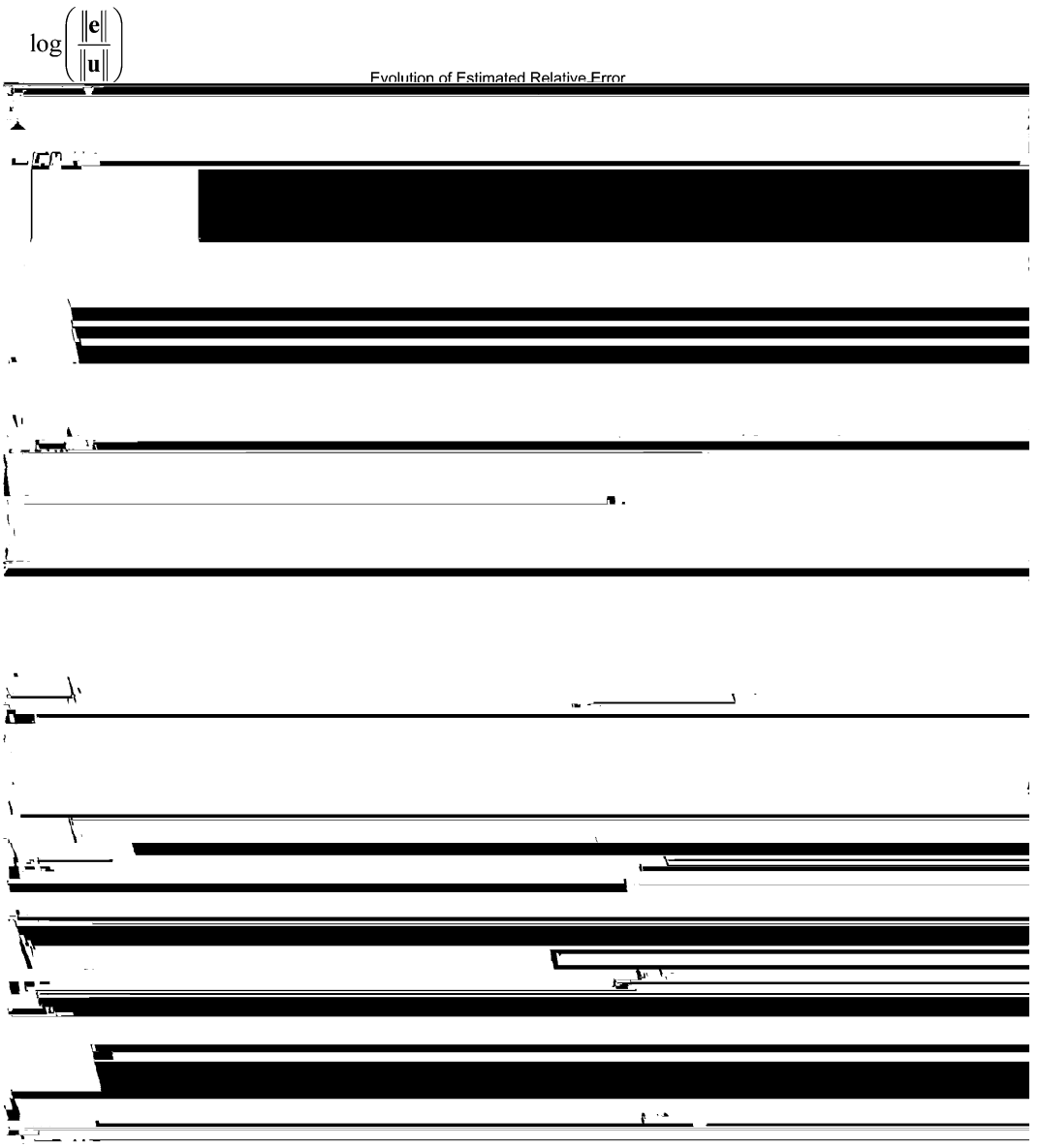

Fig. 16. Convergence of estimated relative error for torus under uniform internal pressure (considering stress error estimation and mesh distortion measure).

In order to consider the effect of mesh distortion as well as that of the relative stress error, the weight function is reconstructed for the parameter study:

$$\left(\frac{1}{f(\vec{x})}-1\right)_{\text{total}} = (1-a)\left(\frac{1}{f(\vec{x})}-1\right)_{\text{stress error}} + a\left(\frac{1}{f(\vec{x})}-1\right)_{\text{distortion}}, \tag{56}$$

where a is a parameter which varies from 0 to 1. Mesh distortion part in Eq. (56) prevents grids from excessively concentrating in the region where the value of the stress error estimation is high (see Fig. 17). Using Eq. (56), the relative error of the torus under uniform internal pressure is depicted in Fig. 16 as the parameter a varies. Also, the logarithmic relative errors are shown in Table 1. In this table, the bold numbers indicate the smallest relative error among the values of error estimators for a fixed number of elements. Fig. 16 and Table 1 show that the relative error oscillates and varies abruptly in some cases as the parameter value a changes. For instance, in 100 elements, the relative errors in the uniform mesh are the same as those in the adjusted mesh ($a = 0.0$) which considers only stress error estimation. Also, there is a large difference between the relative error of $a = 0.0$ and that of $a = 0.1$.

As shown in Fig. 16 and Table 1, it is not easy to select the proper fixed parameter a. But since the computational cost is low for the grid generation including mesh distortion effect, the proper parameter can be selected by the parametric study of relative stress errors with the variation of a. For example, it takes only about 10 s to generate a grid with 100 elements. Fig. 17 shows the mesh configuration of a torus under uniform internal pressure as parameter a is changed in increments of 0.1. Fig. 17(a), $a = 0.0$, are the adjusted mesh excluding mesh distortion. As parameter a increases, the grids turn back to the initial uniform position.

To compare the sensitivity of the mesh distortion effect of the torus with that of the hemisphere, the convergences of estimated relative errors for the spherical shell subject to uniform internal pressure in the uniform mesh, adjusted mesh 1, and adjusted mesh 2, respectively, are compared in Fig. 18. Adjusted meshes 1 and 2 are constructed by using the weight function given in Eqs. (43) and (56), respectively. As shown in Fig. 18, there was small difference in relative errors. This means that the spherical shell problem is less sensitive to mesh distortion than the torus is. Therefore, the effect of mesh distortion does not need to be considered seriously for a hemisphere.

Table 1
Example of torus – relative error $\log(\|\mathbf{e}\|/\|\mathbf{u}\|)$ and number of element for different value of a

Number of element:	16	36	64	100	144	169	256
Uniform mesh	−1.359	−1.935	−2.193	−2.310	−2.460	−2.646	−2.819
$a = 0.0$	**−1.540**	−2.186	−2.116	−2.310	−2.712	**−2.967**	−3.014
$a = 0.1$	−1.533	−2.205	−2.141	−2.575	−2.678	−2.920	−3.049
$a = 0.2$	−1.521	**−2.210**	−2.176	−2.597	−2.654	−2.868	**−3.057**
$a = 0.3$	−1.504	−2.199	−2.217	−2.624	−2.640	−2.821	−3.038
$a = 0.4$	−1.482	−2.175	−2.264	−2.654	−2.638	−2.785	−3.002
$a = 0.5$	−1.457	−2.140	−2.312	−2.687	−2.646	−2.760	−2.961
$a = 0.6$	−1.431	−2.097	−2.352	−2.718	−2.665	−2.746	−2.922
$a = 0.7$	−1.406	−2.050	**−2.371**	**−2.737**	−2.694	−2.742	−2.890
$a = 0.8$	−1.385	−2.000	−2.362	−2.735	−2.732	−2.749	−2.865
$a = 0.9$	−1.369	−1.951	−2.325	−2.705	**−2.774**	−2.764	−2.848

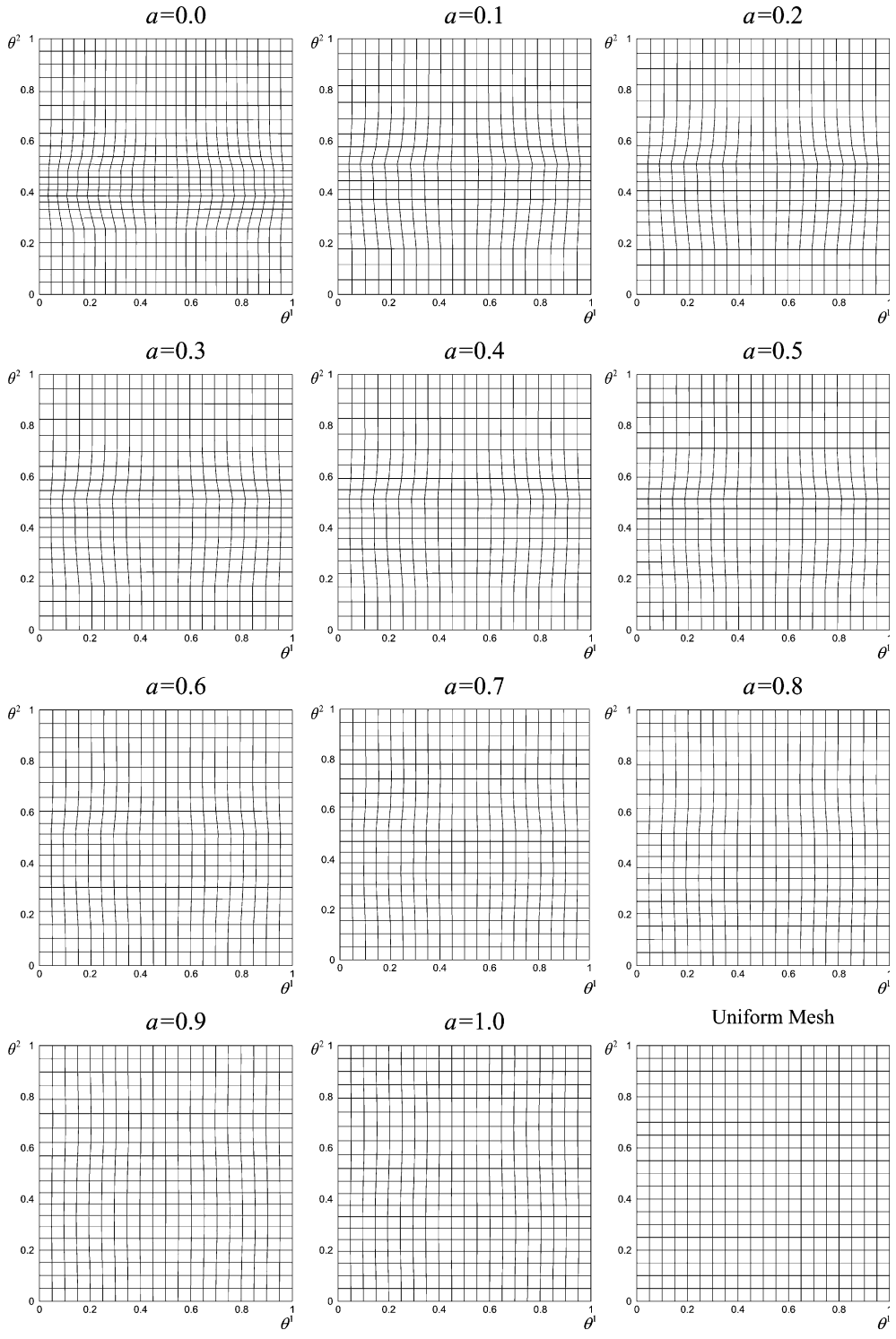

Fig. 17. The mesh configuration of torus under uniform internal pressure according to the change of parameter a.

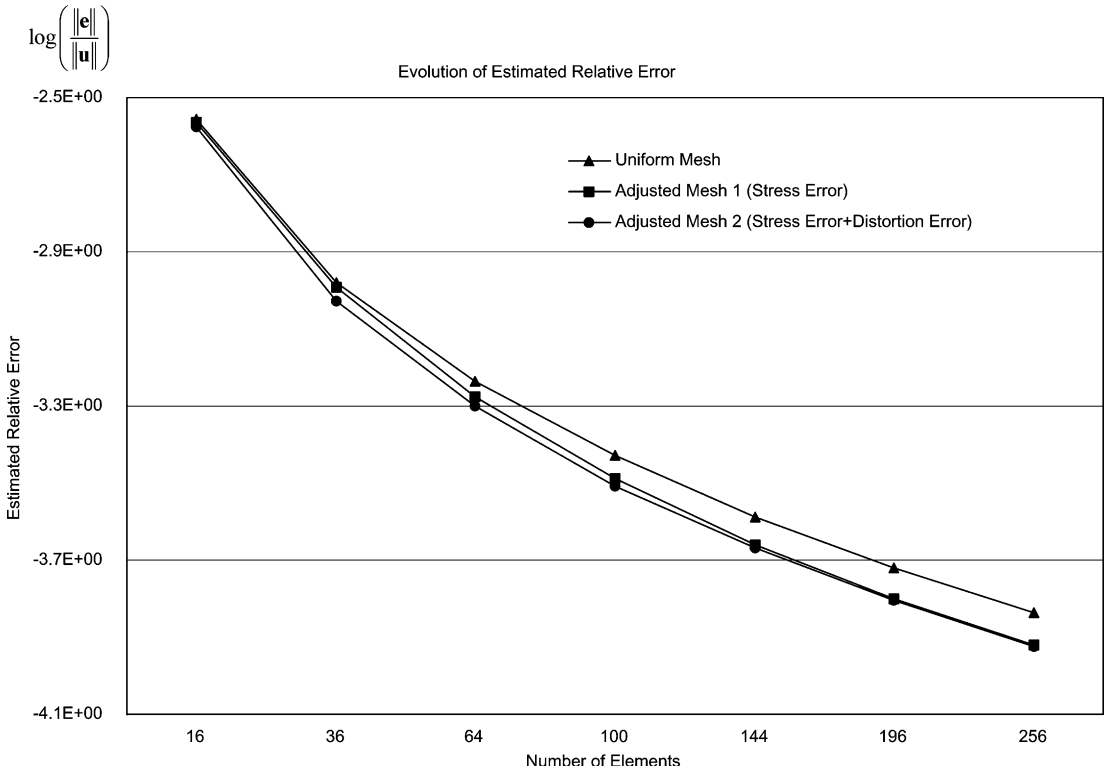

Fig. 18. Convergence of estimated relative error for hemisphere under uniform internal pressure (considering stress error estimation and mesh distortion measure).

6. Conclusion

To compare the convergence rate of the proposed *r*-adaptivity method to those of the uniform refinements, cylinder, sphere and torus problems were studied. To prevent a surface geometry error, the shell surface geometry is exactly represented by B-spline surface tensor patch, which are commonly used in CAD systems. Also, we employed a high performance nine-noded shell element, which is less sensitive to mesh distortion than a four-noded shell element is. The *r*-adaptivity, used in this study, starts from initial uniform mesh and the grids are concentrated in the desired region without any grid tangling. In order to determine the desired region, the value of the stress error estimator computed in a uniform mesh is used as the weight function. By using the grids that are concentrated on the relatively high stress error region, the accuracy of solution is improved. Also, the stress error of the adjusted mesh performs better than that of the uniform mesh configuration in the numerical examples. However, in the torus example, the effect of mesh distortion make the estimated relative error larger than that of uniform mesh. Thus, the severe mesh distortion was prevented by considering the mesh distortion measure as a part of the weight function of cell deformation mapping. A properly chosen parameter value improves the stress performance.

Acknowledgements

This work was supported by the Brain Korea 21 project.

References

[1] J.F. Tompson, N.P. Weatherill, Fundamental concepts and approaches, in: J.F. Tompson, B.K. Soni, N.P. Weatherill (Eds.), Handbook of Grid Generation, CRC press, Boca Raton, FL, 1998, pp. 1–1.
[2] M. Ainsworth, B. Senior, *hp*-Finite element procedures on non-uniform geometric meshes: adaptivity and constrained approximation, in: M.W. Bern, J.E. Flaherty, M. Luskin (Eds.), Grid Generation and Adaptive Algorithm, Springer, New York, 1999, p. 1.
[3] P. Knupp, Mesh generation using vector fields, J. Comput. Phys. 119 (1995) 142.
[4] A.S. Dvinsky, Adaptive grid generation from harmonic maps on Riemannian manifolds, J. Comput. Phys. 95 (1991) 450.
[5] O.C. Zienkiewicz, J.Z. Zhu, N.G. Gong, Effective and practical *h–p* adaptive analysis procedure for the finite element method, Int. J. Numer. Meth. Eng. 28 (1989) 879.
[6] I. Babuška, W.C. Rheinboldt, Adaptive approaches and reliablility estimations in finite element analysis, Comput. Methods Appl. Mech. Engrg. 17/18 (1979) 519.
[7] I. Babuška, Feedback, adaptvivity, and a posteriori estimates in finite elements: aims, theory, and experience, in: I. Babuška, O.C. Zienkiewicz, J. Cago, E.R. Oliveria (Eds.), Accuracy Estimates and Adaptive Refinements in Finite Element Computations, Wiley, New York, 1986, p. 3.
[8] P.L. George, Automatic Mesh Generation: Application to Finite Element Methods, Chichester, New York, 1991.
[9] J. Riccius, K. Schweizerhof, M. Baumann, Combination of adaptivity and mesh smoothing for the finite element analysis of shells with intersections, Int. J. Numer. Meth. Eng. 40 (1997) 2459.
[10] T. Densye de Araújo, D., Roehl D., L.F. Marha, An adaptive strategy for elastic–plastic two-dimensional finite element analysis, in: European Congress on Computational Methods in Applied Science and Engineering, Bareclona, 2000.
[11] H. Askes, A. Rodrígues-Ferran, A combined *rh*-adaptive scheme based on domain subdivision formulation and linear examples, Int. J. Numer. Meth. Eng. 51 (2001) 253.
[12] W. Cao, W. Huang, R.D. Russell, An error indicator monitor function for an *r*-adaptive finite element method, J. Comput. Phys. 170 (2001) 871.
[13] W. Huang, Variational mesh adaptation: isotropy and equidistribution, J. Comput. Phys. 174 (2001) 903.
[14] W. Huang, W. Sun, Variational mesh adaptation II: error estimates and monitor functions, J. Comput. Phys. 184 (2003) 619.
[15] G. Liao, D. Anderson, A new approach to grid generation, Appl. Anal. 44 (1992) 285.
[16] G. Liao, T. Pan, J. Su, A numerical grid generator based on Moser's deformation method, Numer. Meth. Partial Differential Equations 10 (1994) 21.
[17] M. Cho, H.Y. Roh, Development of geometrically exact new shell elements based on general curvilinear coordinates, Int. J. Numer. Meth. Engrg. 56 (2003) 81.
[18] J. Moser, On the volume elements of manifold, Trans. Am. Math. Soc. 120 (1965) 286.
[19] J. Sarrate, A. Huerta, An improved algorithm to smooth graded quadrilateral meshes preserving the prescribed element size, Comm. Numer. Meth. Engrg. 17 (2001) 89.
[20] H. Askes, A. Rodríguez-Ferran, A. Huerta, Adaptive analysis of yield line patterns in plates with the arbitrary Lagrangian–Euleriean method, Comput. Struct. 70 (1999) 257.
[21] P.M. Naghdi, In foundations of elastic shell theory, in: Sneddon (Ed.), Progress in Solid Mechanics, 4, North-Holland, Amsterdam, 1963.
[22] A.E. Green, W. Zerna, Theoretical Elasticity, Oxford University Press, Oxford, 1968.
[23] G. Farin, Curves and Surfaces for Computer Aided Geometric Design: A Practical Guide, Academic Press, New York, 1993.
[24] C. de Boor, On calculating with B-splines, J. Approx. Theory 6 (1972) 50.
[25] M.A. Gutiérrez, R. de Borst, J.C.J. Schellekens, L.J. Sluys, An algorithm for mesh resoning with application to strain localization problems, Comput. Struct. 55 (1995) 237.
[26] G. Pijaudier-Cabot, L. Bodé, A. Huerta, Arbitrary Lagrangian–Eulerian finite element analysis of strain localization in transient problems, Int. J. Numer. Meth. Engrg. 38 (1995) 4171.
[27] O.C. Zienkiewicz, J.Z. Zhu, A simple error estimator and adaptive procedure for practical engineering analysis, Int. J. Numer. Meth. Engrg. 24 (1987) 337.
[28] O.C. Zienkiewicz, J.Z. Zhu, The superconvergent patch recovery(spr) and adaptive finite element refinement, Comput. Methods Appl. Mech. Engrg. 101 (1992) 207.